Master's thesis

NTNU
Norwegian University of Science and Technology
Faculty of Natural Sciences
Department of Physics

Ella Johanne Devold

Characterization of the mechanical properties of pancreatic, breast, and colon tumor models

Master's thesis in Nanotechnology
Supervisor: Catharina de Lange Davies
Co-supervisor: Caroline Einen
July 2022

NTNU
Norwegian University of
Science and Technology

Ella Johanne Devold

Characterization of the mechanical properties of pancreatic, breast, and colon tumor models

Master's thesis in Nanotechnology
Supervisor: Catharina de Lange Davies
Co-supervisor: Caroline Einen
July 2022

Norwegian University of Science and Technology
Faculty of Natural Sciences
Department of Physics

NTNU
Norwegian University of
Science and Technology

ABSTRACT

The dense and rigid extracellular matrix in malignant tumors creates a physical barrier that hinders the delivery of drugs, and thus compromises treatment efficacy. This project has measured the stiffness of three murine tumor models, and related the results to the concentrations of two important ECM constituents: sGAG and collagen.

Micro indentation of tumor sections provided force indentation depth curves, which could be used to estimate spring constants and Young's moduli by curve fitting to Hooke's law and Hertz model. Hooke's law was curve fitted within a 100 μm linear interval, while Hertz model included data from the entire force curve. Young's modulus was also calculated from the shear wave velocity acquired using shear wave elastography. The contents of collagen and sGAG were measured using pre-made assay kits, and provided measurements of the concentrations in μg collagen or sGAG per mg wet weight of the tumor. The concentrations of sGAG provide an indication of the proteoglycan contents in the tumor.

KPC consistantly had the highest stiffness parameters, while CT26 had the lowest. The stiffness parameters for 4T1 varied depending on experimental procedure; indentation data suggested similar stiffness parameters to CT26, and shear wave elastography indicated Young's modulus similar to KPC. Correlation analysis of stiffness parameters and concentrations of collagen and sGAG showed that the collagen concentration increased and sGAG concentration decreased with increasing tumor stiffness. However, except for the correlation between Young's modulus from indentation and sGAG concentration, none of the trends were statistically significant.

SAMMENDRAG

Den tette og stive ekstracellulære matriksen i kreftsvulster danner en fysisk barriere som hindrer tilførsel av medisiner og dermed hemmer kreftbehandling. I dette prosjektet har stivheten til tre tumormodeller fra mus blitt målt og sammenlignet med konsentrasjonen av to viktige bestanddeler av den ekstracellulære matriksen: sGAG og kollagen.

Mikroindentering av kreftsvulstene ga kraft-indenteringskurver som, ved å kurvetilpasse dem til Hookes lov og Hertz-modellen, ga verdier for fjærkonstanten og Youngs modulus. Hookes lov ble kurvetilpasset innenfor et lineært intervall på 100 μm, mens Hertz-modellen inkluderte data fra hele kraftkurven. Youngs modulus ble også beregnet basert på skjærbløgehastigheten som ble målt ved bruk av skjærbølgeelastografi. Innholdet av kollagen og sGAG ble målt ved bruk av ferdige assay-kit, og ga målinger av konsentrasjonen i μg kollagen eller sGAG per mg våtvekt av kreftsvulsten. Konsentrasjonen av sGAG ga en indikasjon på proteoglykaninnholdet i kreftsvulsten.

KPC hadde gjennomgående høyest verdi for stivhetsparametrene, mens CT26 hadde lavest. Stivhetsparametrene for 4T1 varierte avhengig av den eksperimentelle metoden; resultater fra indentering ga stivhetsparametre tilsvarende CT26, mens skjærbølgedataene antydet at Youngs modulus var tilsvarende KPC. Korrelasjonsanalyse av stivhetsparametre og konsentrasjon av kollagen og sGAG viste at kollagenkonsentrasjonen økte og sGAG-konsentrasjonen sank med økt svulststivhet. Med unntak av korrelasjonen mellom Youngs modulus fra indentering og sGAG-konsentrasjonen var ingen av trendene statistisk signifikante.

PREFACE

This master thesis is the final project of the study program Master of Science in Nanotechnology, with a specialization in Bionanotechnology, at the Norwegian University of Science and Technology. The project was executed in association with the Department of Physics.

I am grateful to my main supervisor Catharina de Lange Davies (Professor, Dept. of Physics), for excellent guidance throughout the experimental work and the writing process of this report. I would also like to express my appreciation to my co-supervisor Caroline Einen (PhD student, Dept. of Physics) for providing training and guidance in my experimental work, and assistance in writing the report. She also provided the tumors essential for the experimental work. A special thanks must be given to Astrid Bjørkøy (Senior Engineer, Dept. of Physics), for her great expertise and guidance on the lab equipment, as well as providing the necessary lab training. I am grateful to Rune Hansen (Senior Research Scientist, Sintef) and Naseh Amini (Senior Project Engineer, SURF Technology) for providing valuable assistance in performing shear wave elastography. An additional thanks to Rune for for his assistance in interpreting the results. I would also like to thank my fellow master student from MTNANO, Håkon Wesche, for providing training and guidance in my experimental work. Lastly, I would like to thank all my friends and loved ones for endless patience and support.

The figures in this thesis were created using BioRender.com.

CONTENTS

ABBREVIATIONS

List of all abbreviations in alphabetic order:

- **ATCC** American Type Culture Collection
- **CAF** Cancer-associated fibroblasts
- **DMEM** Dulbecco's Modified Eagle Medium
- **DMMB** Dimethylmethylene blue
- **DPBS** Dulbecco's Phosphate Buffered Saline
- **ECM** Extracellular matrix
- **FBS** Fetal bovine serum
- **GAG** Glycosaminoglycan
- **HA** Hyaluronan
- **HME** Harmonic Motion Elastography
- **NTNU** Norwegian University of Science and Technology
- **PAAm** Polyacrylamide
- **PDAC** Pancreatic ductal adenocarcinoma
- **prf** Pulse repetition frequency
- **rcf** Relative centrifugal force
- **ROI** Region of interest
- **rpm** Revolutions per minute
- **s.c.** Subcutaneous
- **SD** Standard deviation
- **sGAG** Sulfated glycosaminoglycan
- **SWE** Shear wave elastography
- **TME** Tumor microenvironment
- **US** Ultrasonographic

CHAPTER

ONE

INTRODUCTION

Cancer research has long been a highly prioritized research field, but despite significant efforts the mortality rate for many types of cancer remains high, with millions of new cases and cancer-related deaths reported each year [1]. Thus, the challenge of finding a cure for cancer remains. In recent years, the focus has shifted towards understanding the tumor microenvironment (TME) as a complex entity consisting of cancer cells, immune cells, fibroblasts, and the extracellular matrix (ECM).

The TME encompasses the tumor vasculature, infiltrating immune cells, connective tissue, and the ECM [2]. While the TME itself may not be malignant, it contains properties and components that can hinder the delivery of therapeutics to tumor cells and promote cancer formation and progression. Compared to regular tissue, the ECM in tumors is often stiffer, and collagen and proteoglycans overexpressed in solid tumors [3, 4]. The dense and rigid ECM in tumors creates a physical barrier that hinders the delivery of drugs in the TME [5]. Netti et al. (2000) performed a study that investigated the collagen network and its interaction with the proteoglycan matrix within tumors [6]. The study concluded that the resistance to delivery of macromolecule therapeutics in tumors was mainly attributed to the collagen concentration. However, stiffness and concentration of ECM constituents vary among different tumor models, and must be characterized for each tumor model.

This thesis is part of a larger project working with characterizing three murine tumor models, and ultrasound mediated delivery of drug-loaded nanoparticles to tumor models to increase drug delivery. Ultrasound is combined with microbubbles, which oscillate in response to ultrasonic waves. This can assist the drug in crossing the blood vessel wall and physically push it deeper into the extracellular matrix [5]. Characterisation of the mechanical properties of the tumor models is important to study how differences between tumor models may affect the drug delivery. In this project, the stiffness of three murine tumors, KPC, 4T1 and CT26, is investigated, and compared to the levels of collagen and sulfated glycosaminoglycan. A micro indenter was used to obtain force indentation curves, which are curve fitted with Hertz and Hooke's model to obtain the Young's modulus and spring stiffness constant, which is two different measures of stiffness. Shear wave elastography provided another measure of Young's modulus, derived from shear wave velocity. The absorbance was measured after performing Sircol collagen and

Blyscan sulfated glycosaminoglycan assays to calculate the concentration of collagen and sGAG in the tumor samples. The sGAG concentrations provide an indication of the concentrations of proteoglycans in the tumors. The overall aim of the master thesis is to study the association between tumor tissue stiffness and amount of the ECM constituents collagen and sGAG, and to determine the impact of stiffness on drug delivery.

CHAPTER

TWO

THEORY

2.1 Tumor biology

2.1.1 The hallmarks of cancer

Cancer is a malignant tumor, i.e. an abnormal mass of tissue that develops when abnormal cell growth and cellular division results in excessive cellular proliferation [7]. The transformation from normal cells into malignant tumor cells is a multi-step process [8]. In 2000, Hanahan and Weinberg proposed the "Hallmarks of Cancer" theory, identifying six distinct physiological changes necessary for cancer development and growth. These steps include self-sufficiency in growth signals, insensitivity to antigrowth signals, evasion of apoptosis, limitless replicative potential, sustained angiogenesis, and tissue invasion and metastasis. In 2011 Hanahan and Weinberg published 'Hallmarks of cancer: the next generation', where two other distinct attributes of cancer cells which are equally important for the development of cancer were presented [9]. These are avoiding immune destruction, and deregulating cellular energy metabolism. The original and emerging hallmarks of cancer are illustrated in Figure 2.1.1.

2.1.2 The tumor microenvironment

The tumor [1] microenvironment (TME) is composed of various components, as shown in Figure 2.1.2 [4]. The TME include immune cells, fibroblasts, capillaries, and the extracellular matrix (ECM), which contains proteins such as collagen I and fibronectin. Collagen fibers in the ECM provide the tissue with structural strength, and support signal transduction between the cells. Activated fibroblasts, known as cancer-associated fibroblasts (CAFs), secrete cytokines and growth factors and produce an excess of ECM proteins, often leading to desmoplasia and increased tumor stiffness. The density of these components leads to the development of solid stress within the tumor microenvironment, which is divided into growth-induced stress and externally applied stress. These stresses promote tumor progression by altering tissue architecture, promoting invasion, and supporting cancer cell survival.

[1] In this thesis the word tumor refers to malignant tumors, and will be used interchangeably with the word cancer.

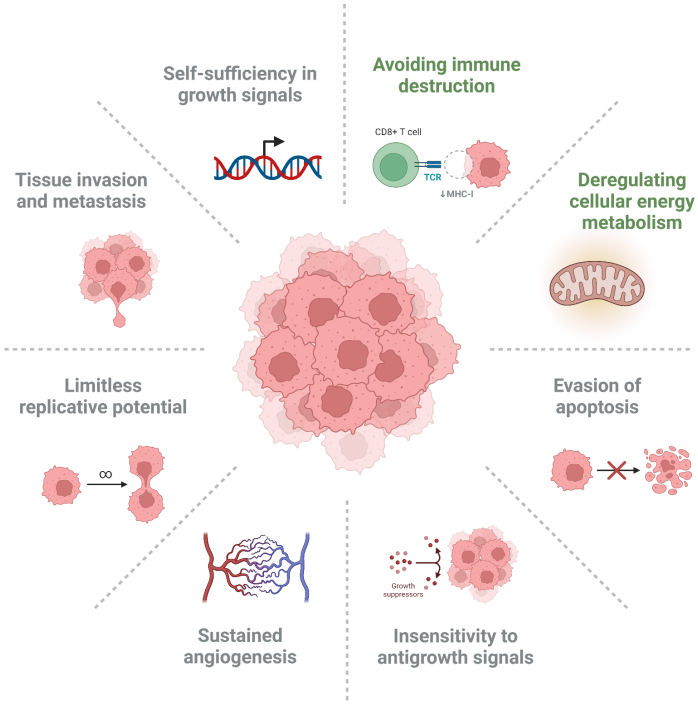

Figure 2.1.1: Figure showing the eight required physiological changes in cancer cells for the formation and growth of tumors, adapted from Hanahan and Weinberg [8, 9]. Original hallmarks are marked in grey, whilst the two emerging hallmarks are marked in green.

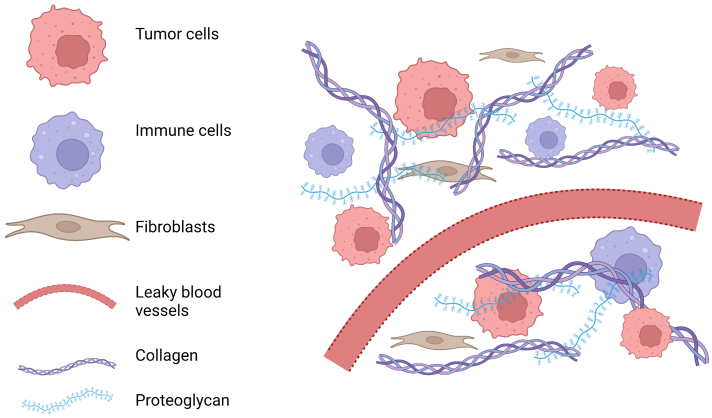

Figure 2.1.2: Illustration shows some of the components of the tumor microenvironment; tumor cells, immune cells, fibroblasts, leaky blood vessels, collagen fibers and proteoglycans.

Tumor growth and progression are sustained by mechanisms such as angiogenesis and co-option of pre-existing blood vessels [10]. However, these vessels are structurally and functionally abnormal, leading to hyper-permeability and impaired circulation. Additionally, unchecked cancer cell proliferation can compress blood and lymphatic vessels, inducing a desmoplastic reaction that results in excessive production of tumor ECM. The tumor microenvironment is highly dynamic, evolving during tumor growth, progression, and treatment, and is strongly coupled with abnormalities within the tumor's vascular and extravascular compartments.

The various components of the TME promote tumor progression in different ways. This thesis will focus on the ECM; its components and mechanical properties.

2.1.3 The extracellular matrix

The shape and mechanical properties of tissues are mainly determined by the ECM, which is composed of three types of molecules: structural proteins, proteoglycans, and adhesive glycoproteins [8]. Structural proteins like collagen and elastin provide strength and flexibility to the ECM, and are embedded in a matrix formed by proteoglycans. Adhesive glycoproteins, such as fibronectin and lamin, enable cell attachment to the ECM. Fibroblasts are the predominant producer of ECM. In the following section we will go further into detail on collagen, proteoglycans, and fibroblasts.

Collagen

Collagen is the most prevalent protein in the human body, and provides tensile strength to tissue [8]. Its structure, shown in Figure 2.1.3, consists of three α-chains forming a triple helix known as the collagen molecule. These molecules then self-assemble into collagen fibrils which, in turn, assemble laterally into collagen fibers. The stability of collagen fibers is ensured by the hydrogen bonds between α-chains and collagen fibrils. There are 15 different types of collagen molecules formed by about 25 different α-chains, with type I being the most abundant. The density and alignment of collagen fibrils vary between different tissues, contributing to distinct mechanical and biological functions [11].

Proteoglycans

The matrix in which structural proteins are embedded into primarily consists of proteoglycans; glycoproteins in which a large number of glycosaminoglycans (GAGs) are covalently bound to a single protein molecule [8]. GAGs are large, anionic carbohydrates characterized by repeating disaccharide units, as illustrated in Figure 2.1.4 [12]. Due to their negative charge they are hydrophilic, attracting both water and cations. This creates the hydrated matrix wherein the structural proteins are embedded. Hyaluronan, which is the salt form of hyaluronic acid, is not sulfated, but the other glycosaminoglycan chains contain sulfate substituents at various positions of the chain [13]. These are called sulfated-glycosaminoglycans (sGAG). Proteoglycans vary greatly in size, depending on the molecular weight of the core protein and the number and length of the carbohydrate chains.

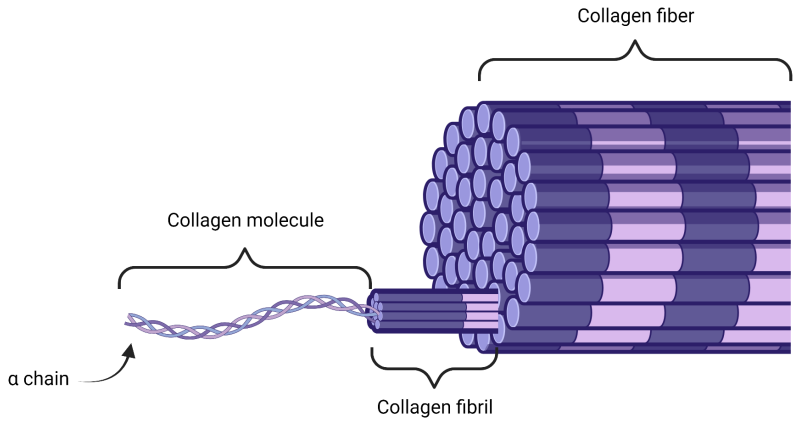

Figure 2.1.3: Schematic of the hierarchical structure of collagen. α chains build up a triple helix, forming the collagen molecules, which nest together to form the collagen fibrils, which again form the collagen fiber.

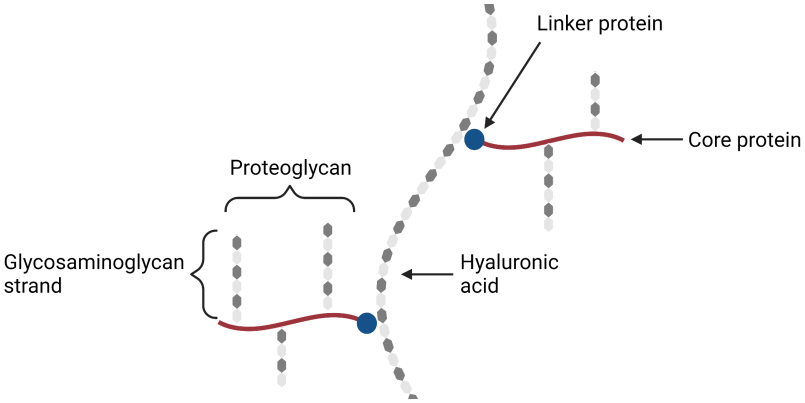

Figure 2.1.4: Example of the structure of a proteoglycan. Glycosaminoglycan chains are covalently bound to core proteins, which again are attached via linker proteins to the central hyalauronan strand.

Fibroblasts

Fibroblasts, shown in Figure 2.1.5, are key regulators of ECM composition and organization [14]. Fibroblasts play an important role in ECM production by producing the ECM's structural proteins, adhesive proteins, and ground substance. In addition, fibroblasts play important roles in maintaining and reabsorbing the ECM, wound healing, inflammation, angiogenesis, and in physiological as well as pathological roles. Additionaly, fibroblasts produce and respond to various paracrine and autocrine signals, such as cytokines and growth factors. In healthy tissue, fibroblasts remain in a quiescent state with negligible metabolic and transcriptomic activities [4].

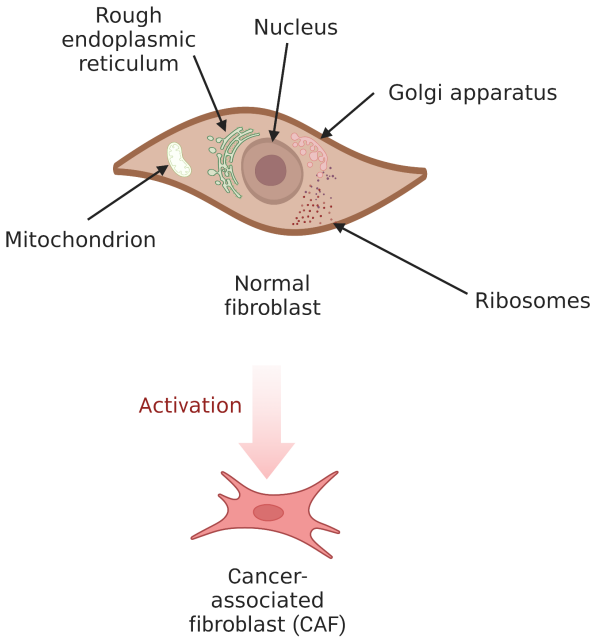

Figure 2.1.5: Illustration of the typical structure of a fibroblast. Depicted are the nucleus, golgi apparatus, ribosomes, mitochondrion, and rough endoplasmic reticulum. Fibroblasts become activated in response to tissue damage.

The extracellular matrix and tumor stiffness

Stiffness is a material property, and refers to its capacity to return to its original shape or form after an applied load is removed [12]. When a material is subjected to a load it experiences stress and strain. Stress is measured as the ratio of force to cross-sectional area, while strain is measured as the ratio of the change in length to the original length along the axial direction, as illustrated in Figure 2.1.6. Biological tissues are modeled as viscoelastic materials, meaning they exhibit both viscous and elastic behaviour when experiencing stress and strain [15]. A generalized stress-strain curve for biological tissues is shown in Figure 2.1.7 [16]. The curve show how changes in the structure of the tissue occur in response to increasing stresses.

In biological tissues, the stiffness is mainly determined by the composition and organization of the ECM [12]. Increased tissue stiffness is a classic characteristic of solid tumors and a critical factor in cancer progression [17, 18]. One of the major contributing factors to stiffening of tumor tissue is increased density of stiffness-promoting matrix components, such as collagen fibers [19, 20]. The condition of overproduction and accumulation of ECM fibers is called desmoplasia. Desmoplasia leads to a continuous stiffening of the tumor [21]. Collagen fibers are secreted from both CAFs and cancer cells [18]. Additionally, CAFs exert contractile forces on the ECM, which modifies the tissue architecture and causes tumor tissue stiffening. This remodeling involves degradation of the ECM and deposition of a new tumor-supporting ECM [22]. Matrix crosslinking is another critical step for stiffening of cancer tissue, and is caused by certain proteins, such as the lysyl

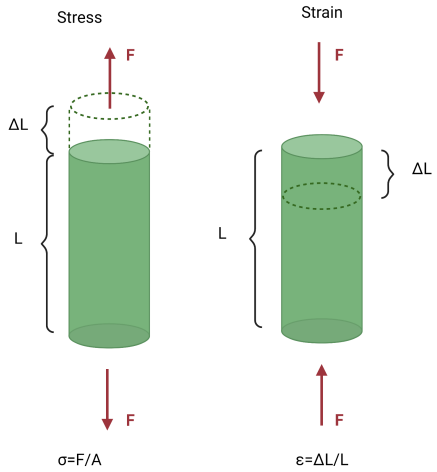

Figure 2.1.6: Illustration showing the concepts, and equations, of stress (σ) and strain (ϵ) as an object is subjected to two equal, but opposite, uniaxial forces, F.

oxidase family proteins. Proteins causing matrix stiffening are secreted by CAFs, cancer cells, and stromal cells.

The mechanical properties of the tumor and host tissue determine how a growing tumor displaces the host tissue and how the host tissue contains or restrains the tumor [17, 23]. When a tumor grows it is restricted by the surrounding healthy tissue, causing compressive forces to accumulate over time. These compressive forces are largest at the center of the tumor. Due to its highly negative charge HA and sGAGs can trap water and swell, and thus resist compressive forces. Hence, HA and sGAG are mostly accumulated in the centre of the cell. The periphery of the tumor experiences compressive forces in the radial direction, but tensile forces in the circumferential direction. Collagen fibers are strongly resistant to tensile loads, which tends to restrict the expansion of tumors. Thus, the collagen density at the tumor periphery is therefore often higher than throughout the tumor tissue.

The role of the extracellular matrix proteins and stiffness in tumor progression

Cancer progression can be enhanced by changes in the ECM within tumor tissue. The ECM plays a crucial role during cell surface receptor signalling, and serves a storage site for growth factors. In addition, it can assist in signalling events using its major adhesion receptors, integrins and proteoglycans. Some of these signaling molecules are growth factors, and thus the ECM can contribute to the continuous growth of malignant cells [17, 24]. The extensive remodeling of the ECM causes signaling through integrins to be altered, causing sustained tumor growth and progression [25].

Studies have revealed that cancer cells exhibit slower proliferation in a softer ECM, while increased matrix stiffness can intensify tumor progression [17]. Moreover, the rigid ECM can directly trigger signaling pathways associated with cell migration, thereby enhancing cell motility and elevating the invasive potential of

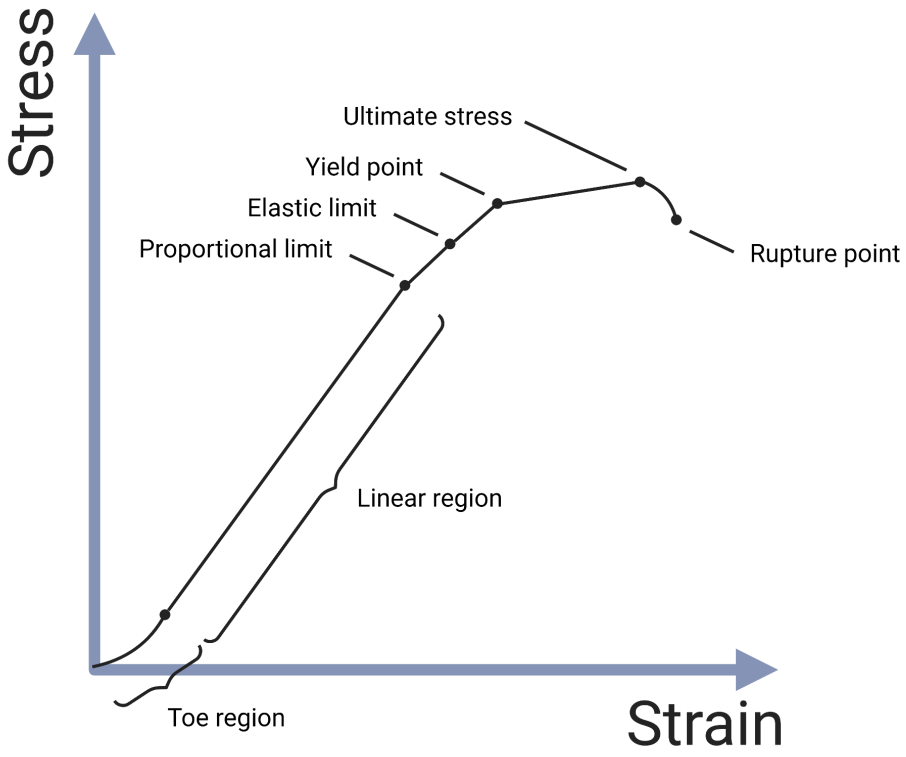

Figure 2.1.7: Generalized stress-strain curve for biological tissues. When the tissue is initially subjected to a load, the gradual increase in stress is described by the toe region. As the stress continues to increase, the curve enters a linear region, which represents the region in which the tissue functions under normal, physiologic stresses. Once the proportional limit is reached the tissue's behaviour becomes non-linear. The elastic limit represents the maximum stress the tissue can endure while still being able to return to its original shape once the load is removed. Upon reaching the yield point, the material starts to rapidly deform until the point of maximum stress, known as ultimate stress. The rupture point occurs at stress level below the ultimate stress, due to the time required for all the tissue to undergo complete failure.

cancer cells.

Elevated matrix stiffness can hinder proper vascularization as the ECM fibers can disrupt endothelial cell-cell junctions, resulting in leaky blood vessels and diminished blood flow [17]. Additionally, the excessive production of ECM and rapid tumor growth can exert compressive forces on both blood and lymphatic vessels within the tumor. This compression, combined with reduced blood flow, can lead to hypoxia. Hypoxia can exacerbate tumor progression by causing alterations in DNA repair mechanisms, cell metabolism, and tumoral immunity [26]. Additionally, changes in transcriptional heterogeneity can contribute to cancer stem cells phenotype, invasion, and resistance to chemo- and radiotherapies [26].

2.2 Methods for stiffness measurements

The following section describes the theoretical background for methods for stiffness measurements used in this project. The tumor stiffness was measured using two different experimental methods - shear wave elastography and micro indentation. Shear wave elastography yields the shear velocity, which is the velocity of a local shear wave produced by a remote mechanical source [27]. This can be used further to calculate the Young's modulus of the sample. The Young's modulus, also known as the elastic modulus, is used to measure the stiffness of materials, and is considered an inherent property, independent of the shape or size of the material [28]. It is calculated as the ratio of stress to strain when an object is subjected to two opposite uniaxial forces. A material with a higher Young's modulus is stiffer, resulting in a smaller strain for the same applied force.

Micro indentation provides force curves which can be used to calculate the spring constant and Young's modulus of the sample by curve fitting with Hooke's law and Hertz model, respectively. These are both models which describe the deformation of a sample when subjected to a force, and will be further described in the following subsections [29, 30]. The spring constant is a measurement of stiffness of a material, and is defined as the ratio of the force affecting the material to the displacement caused by it [29]. Materials with larger spring constants will experience smaller displacements than materials with lesser spring constant when subjected to forces of equal magnitude.

2.2.1 Shear wave elastography

Shear wave elastography (SWE) is an ultrasonographic (US) imaging technique that allows quantification of mechanical and elastic tissue properties [31]. A shear wave is a transverse wave that appears in an elastic medium when subjected to a periodic shear force, as illustrated in Figure 2.2.1 [32]. SWE generates shear waves in tissue using focused acoustic radiation force from a linear US array, which creates local stress and displacement in tissue. The shear waves propagate through nearby tissue in a transverse plane, moving at a slow velocity, which depends on the shear modulus of the material. The propagation of the shear wave causes shear displacements in the tissue. Tissue displacement are monitored using a fast plane wave excitation method, and determined using a speckle tracking algorithm. The shear wave velocity (c_t) is calculated using tissue displacement maps. Equations

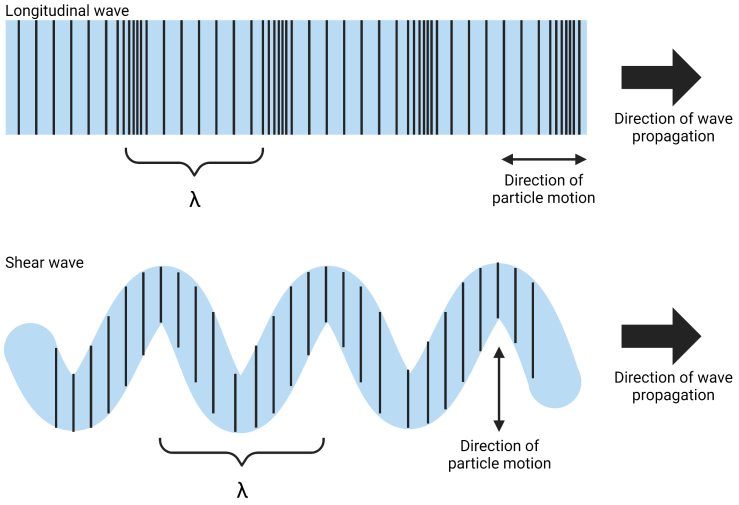

Figure 2.2.1: Illustration of longitudinal wave (top) and shear wave (bottom). A longitudinal wave spreads by successive volume variations of the medium, and the displacement of the medium is parallel to its propagation direction. A shear wave spreads by successive movements that are perpendicular to the direction of propagation.

2.1 and 2.2 show the relation between shear wave velocity and Young's modulus (E):

$$c_t = \sqrt{\frac{\mu}{\rho}} \tag{2.1}$$

$$E = 2\mu(1+\nu) = 2\rho c_t^2(1+\nu) \approx 3\rho c_t^2 \tag{2.2}$$

μ is the shear modulus, ρ is the mass density, and ν is the Poisson ratio [33]. The shear modulus is a measure of a material's ability to resist transverse deformations, and is defined as the ratio of shear stress to shear strain. The Poisson ratio is the ratio of lateral contraction to longitudinal extension of the material under longitudinal tensile stress, illustrated in Figure 2.2.2 [34]. For soft biological tissue, the Poisson ratio is estimated to be approximately 0.5, hence the relation in Equation 2.2 [35]. Biological tissues are considered incompressible materials, wherein the volume remains constant when subjected to an applied force.

Limitations

SWE assumes the material is elastic, incompressible, homogenous, and isotropic [36]. However, soft tissues generally are viscoelastic, inhomogeneous, and anisotropic. Soft tissue elasticity in the human body is nonlinear and dependent on the tissue

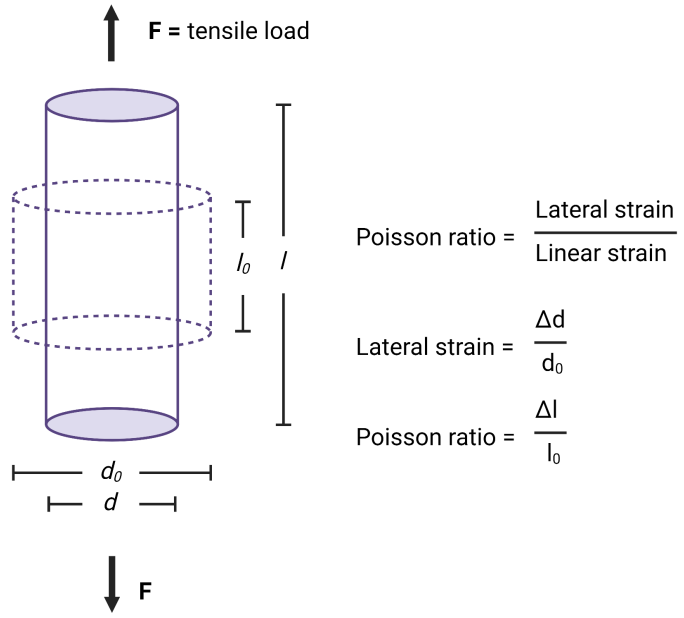

Figure 2.2.2: Illustration depicts the concept and equations for the Poisson ratio as an object is subjected to two equal, but opposite, uniaxial forces, donted as F.

density, strain magnitude, and/or applied excitation frequency. Nevertheless, it is possible to achieve a first-order approximation for elasticity metrics if the viscous forces are ignored, and one assumes linear, elastic solid tissues.

2.2.2 Hooke's law

When a elastic material is subjected to a force, the material stretches or compresses in response to the force [29]. Hooke's law is an empirical law that describes the relationship between the force applied to an elastic object and its resulting deformation. According to Hooke's law, within the elastic limit of a substance, the strain (ϵ) of the material is directly proportional to the applied stress (σ):

$$F = k\Delta d \tag{2.3}$$

F is the applied force, k is the spring constant given in N/m, and Δd is the length of compression/extension.

Limitations

Hooke's law gives accurate results only when the forces and deformations are small [37]. In addition, it only applies within the elastic region of a material, i.e. within the straight segment of the stress-strain curve [29]. Within the elastic region the sample is still able to return to its original shape or size once the load is removed, as described in Figure 2.1.7.

2.2.3 Indentation and Hertz model

The Hertz model, depicted in Figure 2.2.3, assumes a spherical indenter, with radius R, that applies a force F and causes an indentation depth δ on the surface of a sample. The relationship between Young's modulus (E), the force, and indentation depth can be described by the following equation [30, 38]:

$$F = \frac{4}{3}\frac{E}{1-\nu^2}R^{1/2}\delta^{3/2} \tag{2.4}$$

where ν is the Poisson ratio. The spring constant from Hooke's law and Young's modulus from Hertz model is related by the following equation:

$$k = E\frac{A}{L} \tag{2.5}$$

where A is the area over which the force is applied, and L is the nominal length of the material.

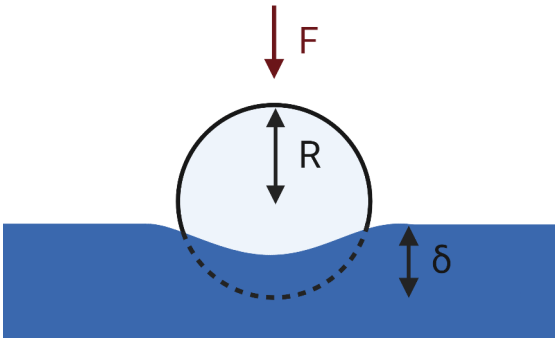

Figure 2.2.3: Figure illustrates the experimental basis for using the Hertz model, where a spherical indenter with radius R applies a force, F, and causes an indentation, δ on the surface of a sample. These parameters can be used to calculate Young's modulus.

Limitations

Hertz model assumes that the sample is an elastic half space [39]. An elastic half space is an isotropic and homogeneous material, extending infinitely in all directions with the top surface serving as a boundary. A biological sample can not be considered an elastic half space. However, if the indentation depth is sufficiently small and the tip radius much smaller than the sample, it is possible to approximate a biological sample as such. According to Buckle's rule, the indentation depth should be limited to 5-10% of the sample thickness to prevent measuring the sample's substrate properties. Additionally, the distance from the tip to the sample's edge should be at least ten times the tip radius, creating an approximation of infinite horizontal extension.

Biological samples fail to meet another requirement of the Hertz model, which assumes that the sample exhibits elasticity [40]. In reality, most biological samples are viscoelastic [36, 41].

Despite the limitations of the model, one can ensure a good model fit for experimental data from biological samples by performing careful experimental control, such as attentive choices of indentation depth and probe sizes [42].

2.3 Colorimetric determination of ECM constituents

2.3.1 Enzymatic extraction of ECM constituents

In order to extract specific proteins from the ECM, enzymes can be used to degrade linker proteins, and thereby freeing the targeted protein [43]. To facilitate enzyme degradation *in vitro*, enzyme activity can be enhanced by adjusting temperature and/or pH.

Pepsin is the main enzyme responsible for protein digestion [44]. It breaks down proteins into smaller peptides and amino acids, which can easily be absorbed in the small intestine. Pepsin depends on activation by an acidic environment, hence, it exhibits its highest efficiency at a pH range of approximately 1.5 to 2. Pepsin can be used to extract soluble collagen from tissue by enzymatic hydrolysis of the ends of the collagen fibers [45].

Papain is a proteolytic enzyme, and can be extracted from the leaves, fruits, roots, and latex of the Carica papaya plant [46]. Proteolytic enzymes are a group of enzymes that facilitate the degradation of long protein chains into peptides, and further into amino acids [47]. By degrading the long protein chains to which sGAG is attached to, papin can be used to extract sGAG from the ECM.

2.3.2 Dye-complex formation

Sirius Red is an anionic dye with a high affinity for collagen [48]. It contains sulfonic acid side chain groups, which bind to specific side chain groups found in collagen. This creates a dye-collagen complex which can be used in colorimetric measurements and analysis.

Dimethylmethylene blue (DMMB) is a dye with a high affinity for sGAG [49]. Electrostatic interactions between the dye and sGAG sulfate group causes the formation of a dye-sGAG complex when mixed in a solution.

2.3.3 Colorimetry

Colorimetry is a technique used to determine the concentration of a specific analyte in a solution [50]. The colorimeter measures the absorbance and transmittance of light that passes through a liquid, and uses Beer-Lamberts law (Equation 2.6) to relate the absorbance to a concentration.

$$A = log\frac{I_0}{I} = \epsilon lc \tag{2.6}$$

A is the absorbance, I_0 is the incident light intensity, I is the transmitted light intensity, ϵ is the absorption coefficient, l is the optical path length, and c is the concentration of the analyte.

In order to get concentration measurements from absorbance readings, you need two things: standards and reference solutions. Standards are solutions with known concentrations of the analyte, while reference solutions consist of buffer solutions without the analyte. If the analyte lacks color or autofluorescence, it needs to be complexed with a dye molecule. A standard curve is then created by correlating the absorbance readings of the standards and reference solutions with their known concentrations. When measuring unknown samples, their absorbance readings can be compared to the standard curve to determine their concentrations.

The accuracy of absorbance measurements relies on the dye having an absorption peak at the wavelength of the incident monochromatic light. As the incident light passes through the sample, the dye absorbs a portion of the light, resulting in a reduction in the intensity of the transmitted light.

2.4 Inter- versus intraheterogenity

Cancers contain morphologically different cells, and multiple tumors of the same type may differ significantly. When a sample population can be divided into subgroups of samples, it is possible to calculte how much of the overall heterogeneity in the population originates from the differences within the subgroups (intraheterogeneity, σ^2_{intra}) versus differences between the subgroups (interheterogeneity, σ^2_{inter}) [51]. Interheterogeneity is defined as the variance of the measured values of all samples. Intraheterogeneity is described by Equation 2.7:

$$\sigma^2_{\text{intra}} = \frac{\sum_{i=1}^{P} \sum_{j=1}^{n_i} (X_{ij} - \overline{X_i})^2}{(N - r)} \tag{2.7}$$

r is the number of subgroups, n_i the number of samples measured in subgroup i, N the total number of samples, X_{ij} the measured value of sample j in subgroup i, and $\overline{X_i}$ is the average measured value of subgroup i.

The proportion of intraheterogeneity relative to the total heterogeneity can be calculated using Equation 2.8:

$$f = \frac{\sigma^2_{\text{intra}}}{\sigma^2_{\text{intra}} + \sigma^2_{\text{inter}}} \tag{2.8}$$

Here, σ^2_{intra} and σ^2_{inter} represent the variances of the measurements due to intraheterogeneity and interheterogeneity, respectively. f ranges from 0 to 1, where a value of 0.5 indicates an equal contribution of both intraheterogeneity and interheterogeneity. A value greater than 0.5 suggests that the contribution to heterogeneity is mainly from within the subgroups rather than between them.

CHAPTER

THREE

METHODS

The tumors used in this project were pancreatic (KPC), breast (4T1), and colon (CT26) tumor models. They were subjected to two methods for stiffness measurements, as well as assays for determining the concentrations of collagen and sGAG. The timeline of experimental procedures is explained in Figure 3.0.1. Tumors were implanted and grown for 14-16 days before harvesting, and shear wave elastography was performed *ex vivo* the same day. Indentation was performed the following day, before the tumors were stored at -80°C for later collagen and sGAG assays.

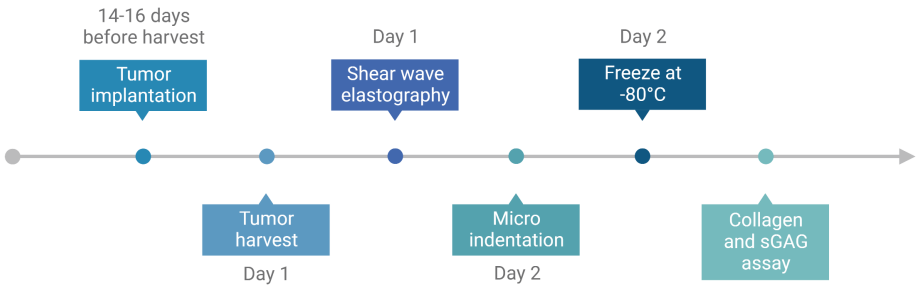

Figure 3.0.1: Timeline of experimental procedures. Tumors were implanted and grown for 14-16 days before harvesting. Shear wave elastography was performed *ex vivo* the same day, and tumors were subsequently stored in the fridge overnight before micro indentation the following day. After indentation, the tumors were frozen at -80°C until collagen and sGAG assays were performed.

3.1 Tumor implantation and harvest

The KPC cancer cells originates from the Department of Radiation Oncology at the Massachusetts General Hospital, where they were isolated from pancreatic

ductal adenocarcinoma (PDAC) tumors in transgenic KPC mice. The KPC cells were cultured in Dulbecco's Modified Eagle Medium (DMEM) (Gibco^{TM} 11960-044, Thermo Fisher Scientific) with 10% FBS, 1% penicillin streptomycin and 0.5% L-Glutamine (G7513, Sigma Aldrich). The 4T1 cells (CRL 2539 ATCC) were cultured in RPMI 1640 Medium in 10% FBS supplemented with 1% penicillin streptomycin. The CT26 cancer cells (CRL-2638, American Type Culture Collection (ATCC)) were cultured in RPMI 1640 Medium (30-2001, ATCC) in 10% fetal bovine serum (FBS) (F7524, Sigma Aldrich) supplemented with 1% penicillin streptomycin (P0781, Sigma Aldrich). All cell lines were kept under exponential growth conditions in 75 cm^2 flasks at 37°C and 5% CO_2 , with subculturing at 70 - 80% confluency twice a week and medium renewal once per week.

During subculturing, the old cell medium was removed before washing the cells twice with 5 mL Dulbecco's Phosphate Buffered Saline (DPBS) (D8537, Sigma-Aldrich). 1 mL 0.25% Trypsin-EDTA (Gibco^{TM} 25200-072, Thermo Fisher Scientific) was added, followed by incubation at 37°C for 3 minutes to detach the cells. Subsequently, the trypsin was neutralized by adding 9 mL fresh cell medium and the cells were pipetted to ensure a homogeneous cell suspension. A certain volume of cell suspension was transferred to new 75 cm^2 flasks with 14 mL cell medium to obtain an appropriate seeding ratio. The CT26 and 4T1 cells were seeded at ratio of 1:20 - 1:30, and the KPC cells at ratio of 1:10 - 1:20.

Prior to implantation of cancer cells in mice, the cells were washed, trypsinzed and resuspended as described above. The cells were then centrifuged for 5 minutes at 1500 revolutions per minute (rpm), the supernatant was removed and cell medium was added to the desired cell concentration. Cells were kept on ice until implantation. In case of the KPC cell line, 200 000 cells in 20 μl cell medium were injected subcutaneous (s.c.) in the right hind leg of B6/albino mice. For 4T1, 10 000 cells in 50 μL cell medium were injected in the right hind leg of a BALB/c mouse. For CT26, 100 000 cells in 50 μl cell medium were injected in the left hind leg of a BALB/c mouse.

After 14-16 days, the mice were euthanized and the tumors harvested. After measuring the size and weight of the tumors, they were stored at 4°C in 50 mL microsentrifuge tubes with cold DPBS (RNBK6918, Sigma Aldrich) with cOmplete protease inhibitor cocktail (11836170001, Roche) to a concentration of one tablet per 10 mL DPBS to minimize tissue degeneration. Cell culture, implantation and harvest were performed by Caroline Einen. All animal experiments were approved by the Norwegian Food and Safety Authority.

3.2 Shear wave elastography

Shear wave elastography was performed *ex vivo* the same day as tumor harvest. Prior to SWE imaging, the tumors were cast in a phantom gel consisting of 0.7% (wt/vol) agarose, with 40% evaporated milk (Tørrleffs), and 4.17 g Sephadex G2580 (Sigma-Aldrich) per liter gel. The phantom provides an environment where the shear waves will propagate in stead of being reflected at the tumor border. For the SWE experiments, a custom-made set-up was used, with a custom-made ultrasound probe and software, and a Verasonics Vantage 256 (Verasonics, Kirkland, WA) ultrasound scanner. Shear waves were generated via an acoustic push

pulse, using 5 MHz, with a pulse length of 200 microseconds (corresponding to 1000 oscillations), and f-number in azimuth of 2.5. Tracking the shear waves was done by using 14 MHz, a shorter pulse of 1-2 oscillations, plane waves, and a pulse repetition frequency (prf) of 10 kHz. Prf refers to the number of ultrasound pulses emitted by the transducer within a specific time frame [52]. Using the plane waves ensures a high prf, which ensures high temporal resolution when tracking the shear waves. The tracking provides a color map of the shear wave velocity (in m/s), and a confidence display generated by the software which indicates the quality of the measurements within the region of interest. Two measurements were taken at two different planes of each tumor. Each measurement was divided into two subsets of data: one with measurements of the waves propagating to the right, and one of the waves propagating to the left. Sample preparation and SWE was performed in collaboration with Rune Hansen and Naseh Amini.

After SWE, the tumors were cut out from the phantom, and stored at 4°C in 50 mL microsentrifuge tubes with cold DPBS with cOmplete protease inhibitor cocktail to minimize further tissue degeneration.

3.3 Micro indentation

Micro indentation experiments was performed the following day of tumor harvest, using a custom-made set-up. The set-up consisted of a stepper motor from Newport (TRB25CC), a custom-made 1 mm spherical indenter, i.e. with radius R = 0.5 mm, and a scale from Sartorius (YAC01ED). Data was acquired and stored using a custom-made LabView script.

The tumors weighing more than 0.2 grams were cut in half along the centre, whilst the tumors weighing less were kept intact due to their small size. This is to limit the indentation depth to 5-10% of the sample thickness, as explained in Section 2.2.3. The samples were placed in a 60 mm × 15 mm polystyrene petri dish with DPBS to prevent dehydration of the tumor.

Indentation was performed at 2 μm/s. Stepper-motor position and weight were continuously recorded throughout the experiment per 100 ms from t = 0 to t = 100 s. This ensured indentation depth of approximately 200 μm. Indentation was performed at five different positions on the tumor or tumor section, with some exception for the smallest tumors to avoid performing measurements too close to the sample's edge to account for the limitations of the Hertz model, as explained in Section 2.2.3. This yielded 10 measurements for the biggest tumors (five measurements per section). For the tumors which were cut in two, indentation was performed on the cut surfaces of the tumor sections.

After indentation, the tumors were rinsed with DPBS and stored at −80°C in 50 mL microsenrifuge tubes for later measurements of collagen and sGAG.

3.4 Data analysis

3.4.1 Shear wave elastrography

Initial processing of the data from SWE was performed by Rune Hansen and Naseh Amini. This yielded the images shown in Figure 3.4.1, where the three

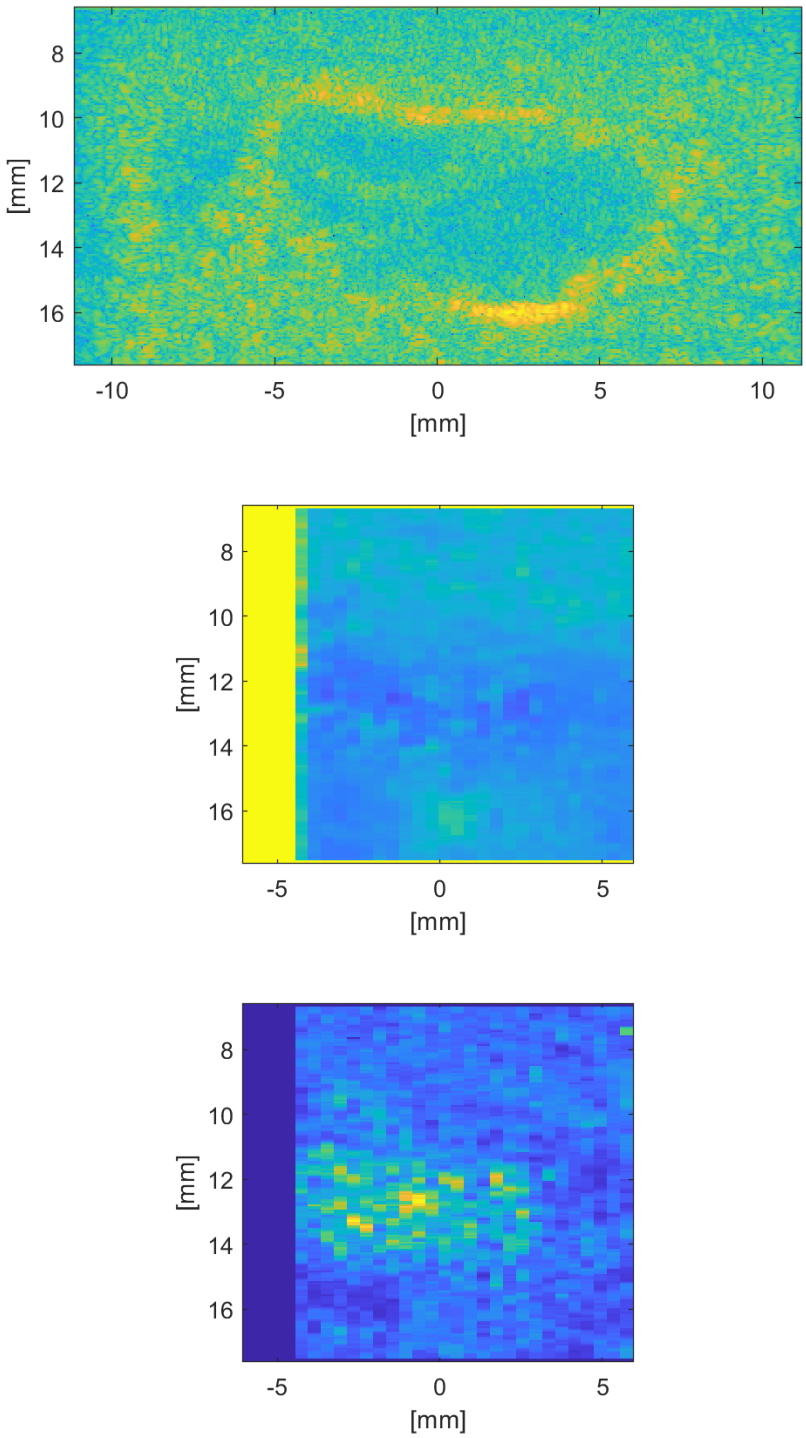

Figure 3.4.1: Example of SWE image. First is the B-mode image of the tumor. The middle and bottom image displays the shear wave velocity and standard deviation for the estimate, respectively. This image originates from a CT26 tumor.

images show the B-mode image of the tumor, and the corresponding shear wave velocity and standard deviation for the estimate. The pixels in the second and third images correspond to measurements of shear wave velocity and SD, ordered as data in a matrix.

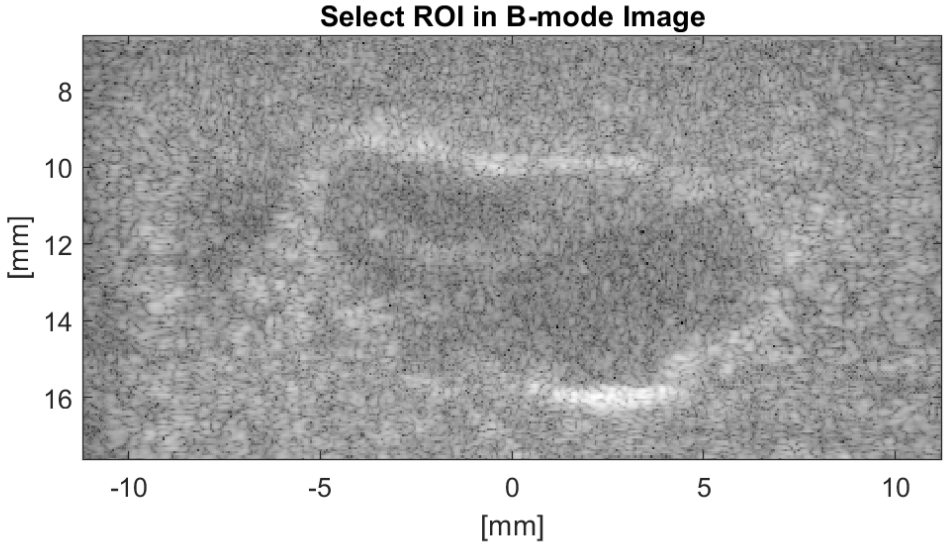

Figure 3.4.2: Example of greyscale B-mode image, originating from the same CT26 tumor as in Figure 3.4.1. The ROI was chosen within this image, and to ensure correct dimensions of the ROI, it was compared to the measurements of the tumor.

Image analysis

Further analysis of the SWE images was performed using the Image Processing Toolbox™ in MATLAB [53]. The MATLAB script used is included in Appendix A. A region of interest (ROI) was established around the tumor in a greyscale version of a B-mode image, shown in Figure 3.4.2, using the measurements performed after harvesting to verify the dimensions were correct. Regions displaying a high standard deviation (SD $>$ 1) in the third image were excluded, as this indicated unreliable measurements. The ROI was transferred to the shear wave velocity image to calculate values for the mean, median, standard deviation, and variance within the ROI.

3.4.2 Micro indentation

The force indentation depth curves were curve fitted to Hooke's law (Equation 2.3) and Hertz model (Equation 2.4) using the Python script in Appendix B, which

also estimated the spring constant and Young's modulus, respectively. Both models were curve fitted to the entire force curve, to include all relevant information. However, as Hooke's law describes the linear relation between force and indentation depth, it was also curve fitted within an interval of 100μm, ranging from 100 to 200 μm. This interval was chosen as it consistently exhibited an approximately linear relationship between force and indentation depth.

The Python script also calculates the P-value and R^2. In model fitting, the P-value determines the significance of the model compared to the null hypothesis, while R^2 is a measure of how well the model describes the data [54].

Correction for evaporation

During micro indentation, the bottom of the petri dish was covered with DPBS to prevent drying of the tumor during indentation. Due to the sensitivity of the indenter, indentation was performed above a petri dish with its bottom covered with DPBS to attain data for potential evaporation during indentation. Distance between the petri dish and indenter tip was varied to account to differences in tumor thickness. In total, 10 such measurements were performed, and linear regression of all data points was performed to find a force curve for evaporation. This force curve subtracted from the initial force curves to correct the data for evaporation. The data from the DPBS indentation experiments and the associated linear regression line is shown in Figure 3.4.3.

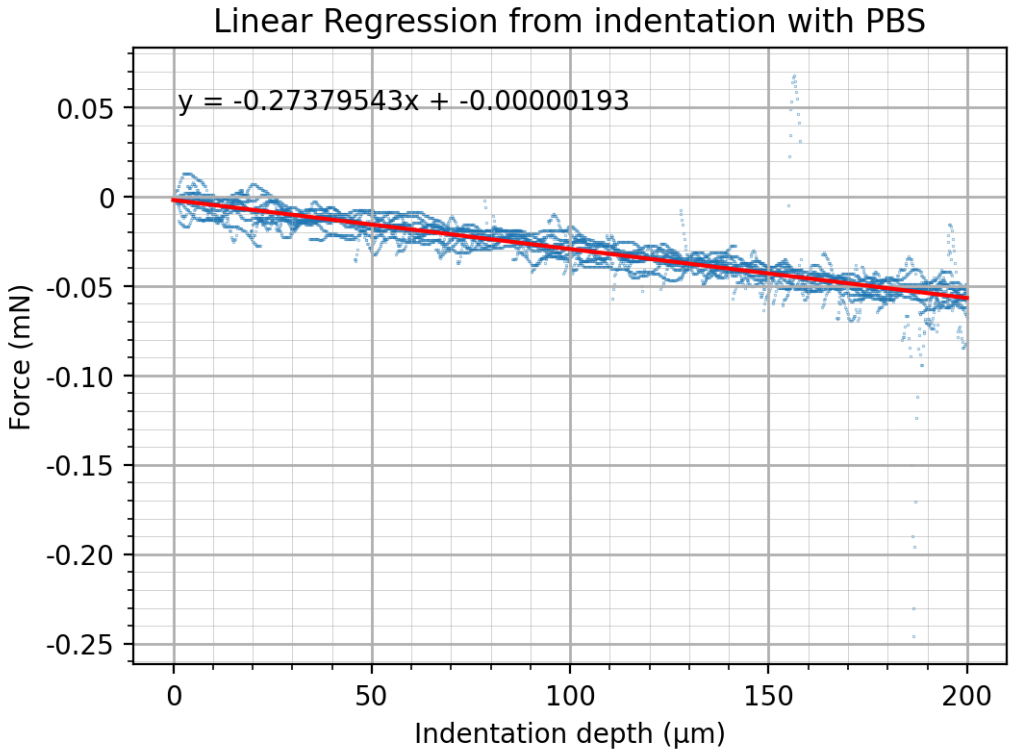

Figure 3.4.3: Data and linear regression line from indentation with a petri dish with DPBS. The linear regression line is used to correct for DPBS evaporation and other experimental errors.

3.5 Colorimetric determination of ECM constituents

3.5.1 Sample preparation

Cold DPBS was added to the 50 mL microsentrifuge tubes to cover the tumors, and the tubes were thawed over ice. After thawing, the tumors were rinsed with DPBS and weighed in 1.5 mL conical Eppendorf tubes using a Sartorius Basic BA 110S balance.

Homogenization was performed in a polystyrene petri dish with a scalpel and a pair of tweezers. To prevent the tumors from drying out during this process, DPBS was used to coat the bottom of the petri dish. A random selection of the sample pieces was transferred to 1.5 mL conical Eppendorf tubes, and weighed. For the collagen assay, sample weight was between 10-15 mg, and for sGAG it was between 20-25 mg. This corresponded to 3-5 tumor pieces for collagen assay, and 5-10 for sGAG. Sample weights for the assays were chosen to ensure that the samples contain an amount of collagen or sGAG that approximately corresponds to the middle of the standard curve [48, 49]. Examples of standard curves for both assays are shown in Figure 3.5.1. All 18 tumors were run in triplicates, resulting in 54 samples in total.

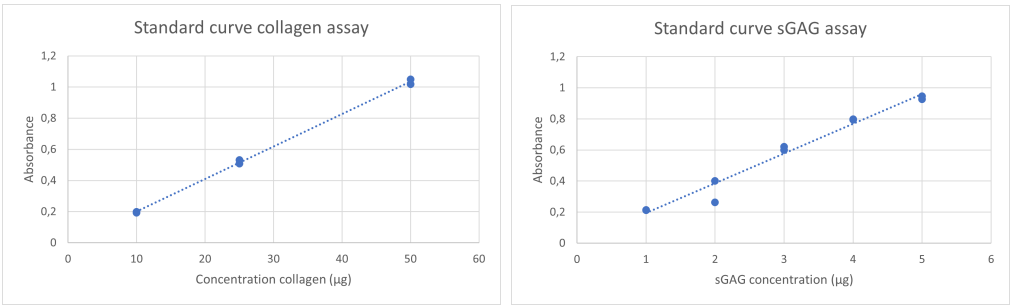

(a) (b)

Figure 3.5.1: Standard curve used to calculate the concentrations of collagen (a) and sGAG (b) in the samples. The collagen standard curve originates from absorbance measurements of standards containing 10, 25, and 50 μg collagen, and the sGAG standard curve originates from absorbace measurements of standards containing 1, 2, 3, 4, and 5 μg sGAG.

3.5.2 Extraction of ECM constituents

Pre-made assay kits from Biocolor were used for this project, specifically the *Sircol - Soluble Collagen assay kit* [48] and the *Blyscan - sulfated Glycosaminoglycan (sGAG) assay kit* [48]. The Sircol kit consists of Sircol Dye Reagent (BB721, Biocolor), Collagen Reference Standard (BB708, Biocolor), Acid-Salt Wash Reagent (BB727, Biocolor), and Alkali Reagent (BB720, Biocolor). The Blyscan kit consists of Blyscan Dye Reagent (BB718, Biocolor), sGAG Reference Standard (BB723, Biocolor), and Dissociation Reagent (BB730, Biocolor).

Collagen

Pepsin (P7012, Sigma Aldrich) was used to prepare a pepsin digestion buffer at a concentration of 0.1 mg/mL in 0.5 M acetic acid. Digestion buffer was added to the sample tubes in a ratio of 1 mg sample to 30 μL buffer. To avoid self-degradation of the enzyme the digestion buffer was used the same day as it was prepared. The samples were incubated overnight at 4°C in a mechanical shaker (KS125basic, IKALABORTECHNIK) at 500 rpm. The following day the samples were centrifuged at 3000 relative centrifugal force (rcf) for 10 minutes using a Eppendorf 5415 R Centrifuge.

A set of 1.5 mL microcentrifuge tubes were labeled as samples, standards and blanks. 100 μL of the supernatant of each sample was transferred to a new set of 1.5 mL conical Eppendorf tubes. 100 μL of digestion buffer was transferred for the reagent blanks. The collagen standards used the 0.5 μg/μL stock solution from the Sircol collagen kit to prepare standard solutions in digestion buffer containing 10, 25 and 50 µg collagen.

1 mL of Sircol Dye Reagent was added to all tubes, and mixing was performed by inverting contents and placing tubes in a mechanical shaker at 500 rpm for 30 minutes. During mixing the the collagen-dye complex formed and precipitated in the solution. After, the tubes were centrifuged at 13.000 rcf for 10 minutes to ensure firm packing of the complexes. The tubes were subsequently drained of the solution containing unbound dye.

700 μL ice-cold Acid-Salt Wash Reagent was added to the tubes to remove residual unbound dye. The tubes were centrifuged at 13 000 rcf for 10 minutes, berfore being carefully drained, only leaving behind a densely packed collagen-dye complex pellet. 1 mL of the Alkali Reagent was added to each tube to release the bound dye from the collagen. To dissolve the dye in the solution, the tubes were vortexed for a few seconds at 5 minute intervals. 200 μL of each solution was added to individual wells of a 96 Costar Clear Microwell. Absorbance measurements followed immediately to avoid dye bleaching.

sGAG

The digestion buffer was prepared by adding 400 mg Sodium Acetate (104H0293, Sigma Aldrich), 200 mg EDTA Disodium Salt Dihydrate (0533C338, Amresco), and 40 mg L-cysteine Hydrochloride (107H0028, Sigma Aldrich) to 50 mL 0.2 M sodium phosphate buffer, and stirred on a hot magnetic stirrer. The pH was adjusted to 6.4, and when all the salts had dissolved, 250 μL of Papain from papaya latex (P3125-100MG, Sigma Aldrich) was added. To avoid self-degradation of the enzyme, the digestion buffer was used within one week of preparation. 1 mL of the papain buffer was added to the samples, and they were incubated in a thermally regulated heating block at 65°C overnight. The following day the samples were centrifuged at 10.000 rcf for 10 minutes.

A set of 1.5 mL microcentrifuge tubes were labeled as samples, standards and blanks. 50 μL of the supernatant of each sample and 50 μL of the digestion buffer was transferred to a new set of 1.5 mL conical Eppendorf tubes. 100 μL of digestion buffer was transferred for the reagent blanks. The sGAG standards used the 0.1 μg/μL stock solution from the Blyscan sGAG kit to prepare standard solutions in digestion buffer containing 1, 2, 3, 4 and 5 µg sGAG.

1 mL of Blyscan Dye Reagent was added to each tube, and the contents of the tubes were mixed by inverting and mechanical shaking at 300 rpm for 30 minutes. The tubes were subsequently centrifuged at 13 000 rcf for 10 minutes to firmly pack the sGAG-dye complexes. The tubes were drained for unbound dye solution, and 0.5 mL of Blyscan Dissociation Reagent was added to them. The tubes were vortexed at 5 minute intervals to release the bound dye into the solution. When all the dye was dissolved, the tubes were centrifuged at 13 000 rcf for 5 minutes to remove foam. 200 μL of each sample, standard and reference were added to individual wells of a 96 Costar Clear Microwell. A small pipette tip dipped in 70% ethanol was used to remove bubbles from the surface of the solutions before absorbance measurements. Absorbance measurements followed immediately to avoid dye bleaching.

3.5.3 Absorbance measurements

The Spectramax i3x plate reader was used in conjunction with the Softmax Pro 6.5.1 software to perform absorbance readings. For the collagen samples and their associated standards and blanks, the plate reader was set to endpoint absorption measurements with a wavelength of 556 nm. For sGAG, the plate reader was set to endpoint adsorption measurements with a wavelength of 656 nm. Following the measurements, the software generated a standard curve relating the absorbance values of the unknown samples and their concentration in μg collagen or sGAG. Subsequently, this concentration was adjusted, taking into account the sample volume in the microwells, dilutions performed during the assay, and the weight of the tumor pieces. As a result, the final concentration was expressed as μg collagen or sGAG per mg wet weight of the tumor.

3.6 Statistical analysis

All statistical analysis and plots were made in Graphpad Prism 9. All results were subjected to outlier identification and removal, by a built-in outlier identification analysis in Prism named ROUT with Q = 1%. The ROUT method fits a model to the data using a robust method where outliers have little impact [55]. It subsequently uses a new outlier detection method, based on the false discovery rate, to decide which data points are far enough from the prediction of the model to be classified as outliers. Q denotes the maximum desired false discovery rate, hence Q=1% means that it is only acceptable that 1% of all outliers found are false outliers.

To determine the statistical significance an Ordinary one-way ANOVA test with a $p < 0.05$ was done using Prism. Subsequently, a Tukey's multiple comparison test with $\alpha = 0.05$ was used to identify the significance between the tumor model means. Table 3.6.1 provides a summary of the asterisk notation used to denote statistical significance.

Correlation analysis was performed on the data to calculate the Pearson correlation coefficient (r) and assess significance. In addition, a linear regression line was fitted to the correlation data. The statistical tests were deemed statistically significant for p-values less than or equal to 0.05. A Pearson r value between

Table 3.6.1: Table showing the asterisk notations used to denote statistical significance in Prism.

Symbol	**Meaning**	**P value**
****	Extremely significant	< 0.0001
***	Extremely significant	0.0001 - 0.001
**	Very significant	0.001 - 0.01
*	Significant	0.01 - 0.05
ns	Not significant	≥ 0.05

± 0.1 and 0.3 is considered a small correlation, between ± 0.3 and 0.5 a medium correlation, and between ± 0.5 and 1 it is considered large.

Several tests of inter- versus intra tumor heterogeneity were performed as described in Section 2.4. This was done for the spring constant, Young's modulus, and the collagen and sGAG density. In the analysis, the heterogeneity within each tumor was defined as the intraheterogeneity, while the interheterogeneity was defined as the heterogeneity between the tumors of same type. To assess the statistical significance, an Ordinary one-way analysis of variance (ANOVA) test was conducted using Prism, with a significance level set at $p < 0.05$.

The mean stiffness measurements and mean concentrations of collagen and sGAG for each tumor model is based on the mean of 6 tumors. Table 3.6.2 show the number of samples from which the mean per tumor was calculated from.

Table 3.6.2: Table showing the number N of samples per tumor for all experimental procedures. For the indentation measurements, the tumors weighing more than 0.2 grams were cut in two, and both sections were subjected to indentation. This provided more measurements.

Experimental procedure	**N**
Indentation (m $>$ 0.2 g)	10
Indentation (m $<$ 0.2 g)	5
Shear wave elastography	4
Collagen assay	6
sGAG assay	6

CHAPTER

FOUR

RESULTS

4.1 Tumor characteristics

The 18 tumors used in this project are listed in Appendix C, with the corresponding weights and dimensions. 4T1 and CT26 were the largest tumors, with tumor weight ranging from 0.2909 to 0.5766 grams for 4T1, and 0.1384 to 0.5715 grams for CT26. The KPC tumors were smaller, with tumor weight ranging from 0.0393 to 0.1692 grams.

4.2 Assessing curve fit parameters

Figure 4.2.1 show examples of force curves obtained by using the micro indenter on a KPC (Figure 4.2.1a), 4T1 (Figure 4.2.1b), and CT26 (Figure 4.2.1c) tissue section. The force curves are corrected for DPBS evaporation as explained in Section 3.4.2. Only the approach curve (red) is included, as well as the model fit curves for Hertz model (orange) and Hooke's law (blue and green). The blue curve is curve fitted to the entire curve, while the green is only curve fitted within 100 to 200 μm indentation depth. This interval was chosen as it generally showed a high degree of linearity for all three tumor models. As Hooke's law describes a linear relation between force and distance, only the data from within the interval is included [29]. Data from Hooke's law curve fitting to the entire force curve can be found in Appendix E.

As can be seen from the force curves in Figure 4.2.1, the curve fitting of Hertz law to the force curves of KPC and 4T1 tumors is better than Hooke's law. The CT26 force curves were generally linear, both within the interval and throughout the entire curve, and thus showed a good model fit with the linear Hooke's law, as seen in Figure 4.2.1c. These observations are confirmed by the R^2 values, presented in Table 4.2.1.

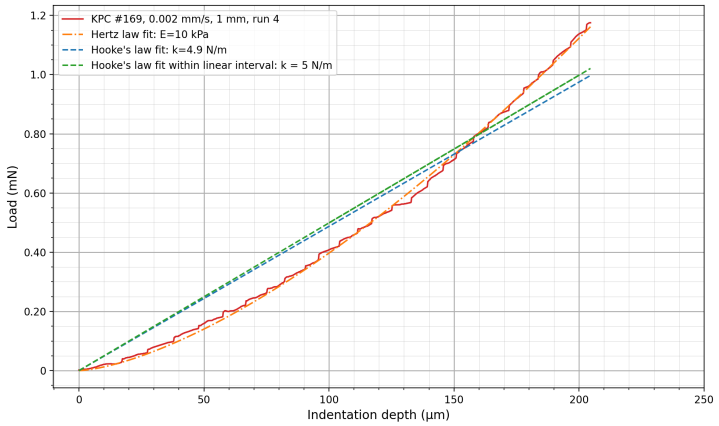

(a)

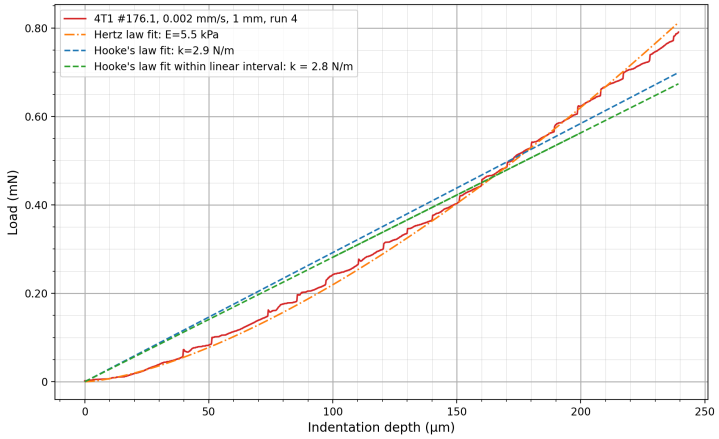

(b)

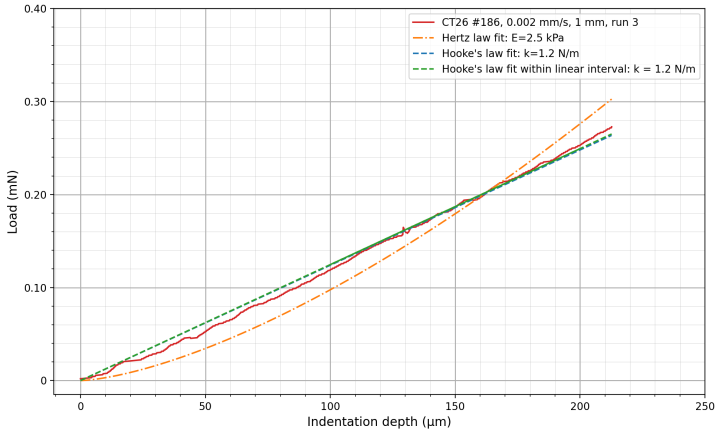

(c)

Figure 4.2.1: Examples of force curves obtained by using the micro indenter on a KPC (a), 4T1 (b), and CT26 (c) tissue section. The red line is the force curve, corrected for DPBS evaporation. The orange curve is the Hertz model fit. The blue and green curves are the Hooke's law model fit curves, calculated for the entire force curve and within the interval 100 to 200 μm indentation depth, respectively. All indentation experiments were performed with an indenter with r = 0.5 mm, at 0.002 mm/s speed, with 200μm indentation depth.

Table 4.2.1: Table showing the R^2 and P-value for the Hooke's law and Hertz model fit to the force curves obtained from micro indentation. The values are mean values, calculated from the mean values of the individual tumors of the same tumor model. The Python script used for calculating the values are included in Appendix B.

Tumor model	R^2	**P-value**
Hooke's law within linear interval		
KPC	0.9082	0.3574
4T1	0.9296	0.3751
CT26	0.9138	0.3836
Hertz model		
KPC	0.9875	0.3514
4T1	0.9811	0.3293
CT26	0.9041	0.2991

4.3 Spring constant - Hooke's law

The results from indentation were subjected to ROUT method with Q=1%. 1 outlier was identified, and removed from the data set. The outlier originated from a CT26 tumor. Outliers from all data sets are included in Appendix D. The force curve for the outlier removed from the indentation data set is also included.

Figure 4.3.1 shows the spring constant for all three models, measured in N/m. The spring constant is derived from the model fit of Hooke's law to the 100 μm linear interval of the force curve. The KPC tumors had a significantly higher spring constant than 4T1 and CT26. There was no significant difference between 4T1 and CT26, meaning their spring constants were similar. The min-max range, median, mean and standard deviation of the spring constant were found to be [3.044-5.365, 4.496, 4.342 $\pm$ 0.9372] for KPC, [0.8417-2.263, 1.386, 1.472 $\pm$ 0.5237] for 4T1, and [0.7020-1.323, 0.9121, 0.9415 $\pm$ 0.2369] for CT26. Compared to the results from the entire force curve, included in Appendix E, the mean spring constant calculated from within the chosen interval is 0.159 N/m higher for KPC, 0.07 lower for 4T1, and 0.0315 higher for CT26.

4.4 Young's modulus - Hertz model and shear wave velocity

Young's modulus was obtained by Hertz model curve fitting to the force curve from indentation, and from the shear wave velocities measured in shear wave elastography. The shear wave velocities were converted to Young's modulus with the assumption that the phantom had a mass density of 1000 kg/m^3, similar to water, and a Poisson ratio of 0.5. This yields the relation given in Equation 2.2.

The results from the SWE were subjected to ROUT method with Q=1%. 4 outliers were identified and removed from the data sets. All outliers originated from the same 4T1 tumor, and were similar to each other, about twice as high as the other results.

Figures 4.4.1a and 4.4.1b shows the Young's modulus from the Hertz model

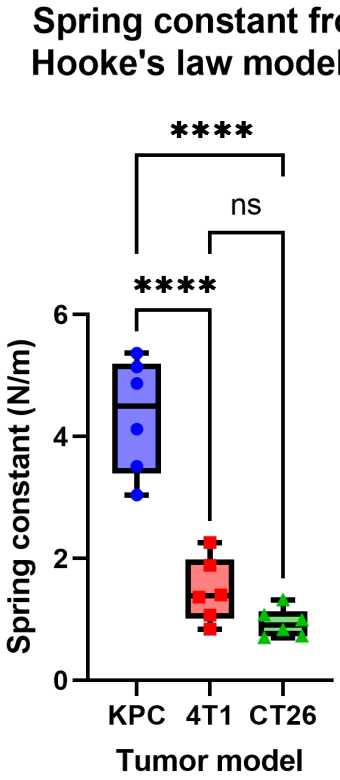

Figure 4.3.1: The spring constant of the tumor models in a box plot. Whiskers represents the minimum and maximum values, and the box is the 25-75%. The median is depicted by a horizontal line crossing the box. Each individual point within the box plot represents the mean value of one tumor. The presence of asterisks between the boxes indicates the statistical significance between the respective data sets, as explained in Table 3.6.1.

fit to indentation data, and from SWE, respectively. In Figure 4.4.1a, Young's modulus for KPC is significantly higher than for both 4T1 and CT26. This trend is similar to that of the spring constants in Figure 4.3.1. CT26 and 4T1 have a similarly low Young's modulus, thus there is no statistical significance between the two data sets. In Figure 4.4.1b, KPC and 4T1 have a similarly high Young's modulus, which is significantly higher than that of CT26. The min-max range, median, mean and standard deviation of Young's modulus is shown in Table 4.4.1. Comparing the results from the two methods with each other show that Young's modulus measured by indentation is much lower than the one measured by SWE.

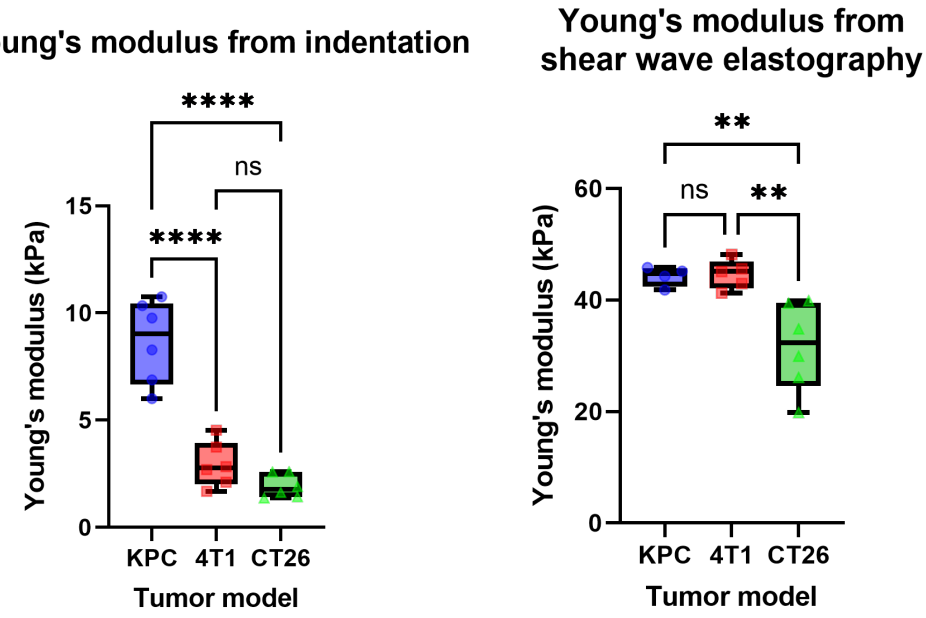

(a) (b)

Figure 4.4.1: Young's modulus from Hertz model curve fitting to indentation force curves (a) and from shear velocity measured in shear wave elastography (b) in box plots. Whiskers represents the minimum and maximum values, and the box is the 25-75%. The median is depicted by a horizontal line crossing the box. Each individual point within the box plot represents the mean value of one tumor. The presence of asterisks between the boxes indicates the statistical significance between the respective data sets.

Table 4.4.1: Table showing the min-max, median, and mean value with standard deviation for Young's modulus from indentation and shear wave elastography.

Tumor model	Min	Max	Median	Mean ± SD
Young's modulus (Hertz)				
KPC	6.004	10.76	9.021	8.671 ± 1.940
4T1	1.687	4.529	2.764	2.933 ± 1.050
CT26	1.371	2.593	1.766	1.917 ± 0.5510
Young's modulus (SWE)				
KPC	41.81	45.84	44.73	44.28 ± 1.767
4T1	41.27	48.16	45.15	44.64 ± 2.640
CT26	19.80	39.88	32.38	31.67 ± 7.899

4.5 Concentration of ECM components

The results from collagen and sGAG assays were subjected to ROUT method with Q=1%. 6 outliers were identified and removed from the collagen data set. All outliers originated from CT26 tumors. The significant deviation to the rest of the group is suggested to originate from experimental error. 0 outliers were identified from the sGAG data set.

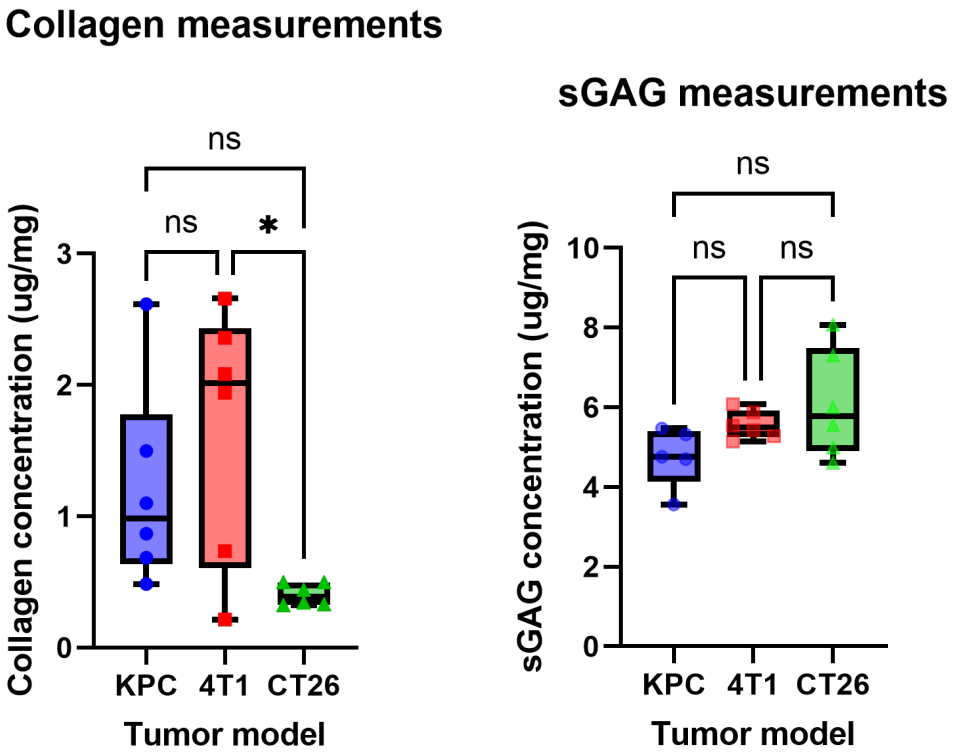

(a) Collagen measurements.

(b) sGAG measurements.

Figure 4.5.1: Amount of collagen (a) and sGAG (b) per mg tumor in a box plot. Whiskers represents the minimum and maximum values, and the box is the 25-75%. The median is depicted by a horizontal line crossing the box. Each individual point within the box plot represents the mean value of one tumor. The presence of asterisks between the boxes indicates the statistical significance between the respective data sets.

Collagen

Figure 4.5.1a presents the collagen concentrations in the tumor samples after removing outliers. There was a significantly higher concentration of collagen in 4T1 compared to CT26. There was no statistical significance between KPC and 4T1, and KPC and CT26, meaning the collagen concentrations in the KPC tumors was comparable to both tumor models. The min-max range, median, mean and standard deviation of μg collagen per mg tumors were found to be [0.4851-2.615, 0.9853, 1.209 $\pm$ 0.7728] for KPC, [0.2160-2.659, 2.013, 1.666 $\pm$ 0.9681] for 4T1, and [0.3230-0.3980, 0.3921, 0.4057 $\pm$ 0.08284] for CT26.

sGAG

Figure 4.5.1b presents the sGAG concentrations in the tumor samples after removing outliers. There was no statistical significance between the data sets, meaning the concentrations of sGAG were similar between the tumor models. The min-max range, median, mean and standard deviation of μg sGAG per mg tumors were found to be [3.563-5.474, 4.765, 4.765 $\pm$ 0.7524] for KPC, [5.142-6.080, 5.484, 5.556

± 0.3576] for 4T1, and [4.615-8.070, 5.780, 6.089 ± 1.348] for CT26.

4.6 Correlations in measurement data

The correlation matrix in Figure 4.6.1 shows the Pearson correlation coefficient (r) between weight, Young's modulus, spring constant, and concentrations of collagen and sGAG. The correlation coefficients are calculated from all data, without differentiating between tumor models. The following section will go further into detail on the correlations.

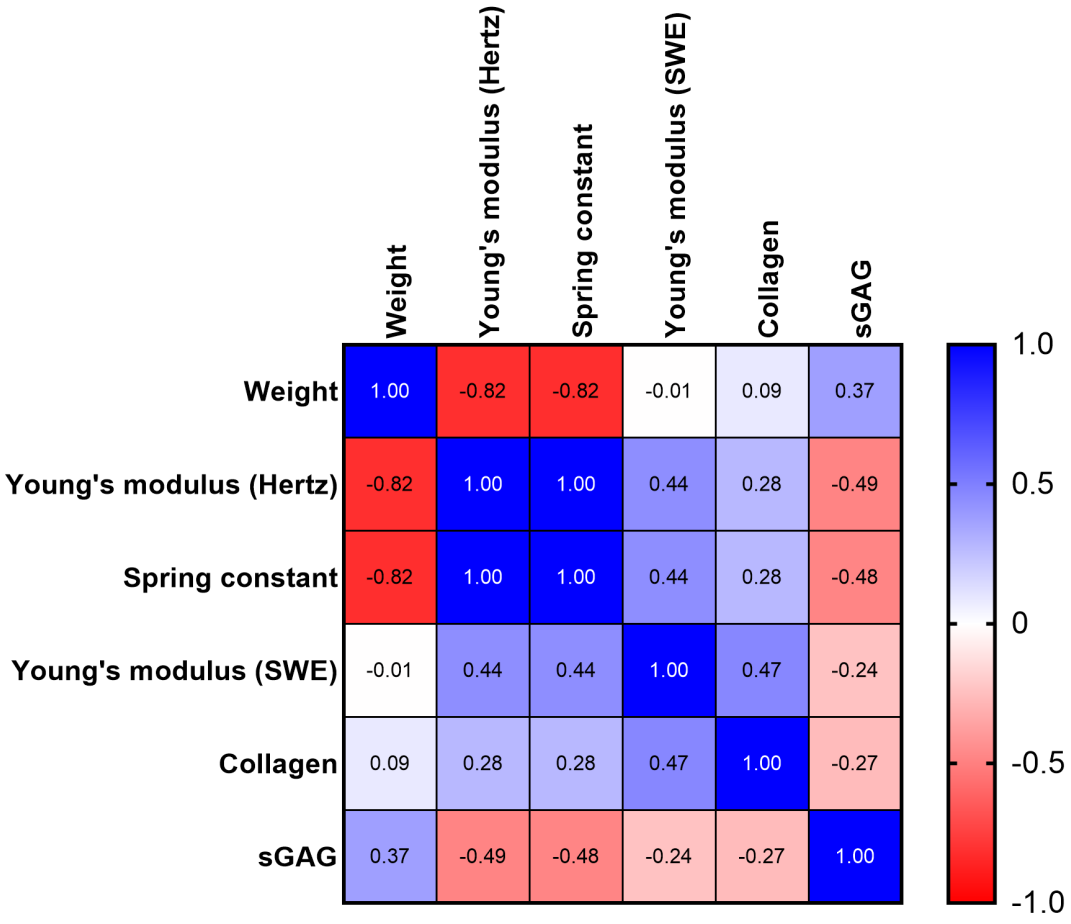

Figure 4.6.1: Correlation matrix showing the correlation coefficient between weight, Young's modulus, spring constant, and concentrations of collagen and sGAG. A correlation coefficient equal to 1 indicates a strong positive relationship, equal to -1 indicates a strong negative relationship, and equal to zero indicates no relationship at all.

4.6.1 Correlation between stiffness measurements

The scatter plots in Figures 4.6.2a, 4.6.2b and 4.6.2c show the correlation plots between the spring constant and Young's modulus from indentation, spring constant and Young's modulus from SWE, and Young's modulus from indentation

SWE, respectively. Data points of the same color corresponds to mean values for individual tumors of the same tumor model. Individual regression lines for all tumor models are also included, in addition to a linear regression line for all data points. As can be seen from Figure 4.6.2a, there is a significant large positive correlation between the data from indentation (r=0.9993, $p < 0.0001$). These calculations originate from the same data sets. Thus, they exhibit similar trends in the following correlation plots. Figure 4.6.2b and 4.6.2c show a large positive correlation between the results from indentation and SWE for KPC and 4T1. CT26 show a medium negative correlation between spring constant and Young's modulus from SWE, and a small negative correlation between Young's modulus from indentation and SWE. The linear regression lines for all data sets show a medium positive correlation. However, the correlations are not statistically significant for any plots.

4.6.2 Correlation between stiffness measurements and measurements of collagen and sGAG

Figure 4.6.3 shows the scatter plots of stiffness measurements and concentrations of collagen. The data points represents mean values for each tumor. Linear regression lines for all data points and for individual tumor models are included. As can be seen from all plots there is a strong positive correlation between stiffness measurements and collagen concentration for KPC tumors. The 4T1 tumors generally show a small negative correlation between the parameters. In Figure 4.6.3a there is a small positive correlation for CT26, but Figure 4.6.3b show no correlation between the indentation data and collagen concentration for CT26 (r = -0.01297). In Figure 4.6.3c, there is a medium negative correlation for CT26. The regression line from all data points show a small positive correlation in Figures 4.6.3a and 4.6.3b, and a medium positive correlation in Figure 4.6.3c. However, the correlations are not statistically significant for any plots.

Figure 4.6.4 shows the scatter plots of stiffness measurements and concentrations of sGAG. The data points represents mean values for each tumor. Linear regression lines for all data points and for individual tumor models are included. As can be seen from Figures 4.6.4a and 4.6.4b, there is no correlation between the indentation results and sGAG concentrations for the KPC tumor model (r = -0.02921 and r = -0.05331, respectively). 4T1 show a medium positive correlation in Figure 4.6.4a, and a small positive correlation in Figure 4.6.4b. CT26 show a consistently small negative correlation. The regression line based on data for all tumor models show a medium negative correlation, which for Figure 4.6.4b is statistically significant (r = -0.4851, p = 0.0484). As can be seen from Figure 4.6.4c, there is a medium negative correlation between Young's moduli and sGAG concentrations for KPC, a small negative correlation for 4T1, and a small positive correlation for CT26. The regression line for all data points show a small negative correlation. However, none of the results are statistically significant.

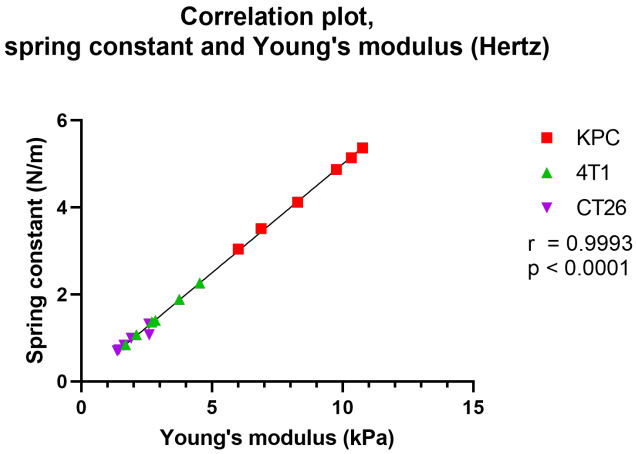

(a)

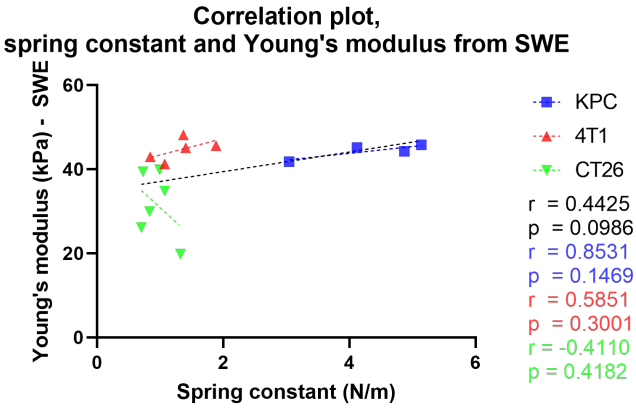

(b)

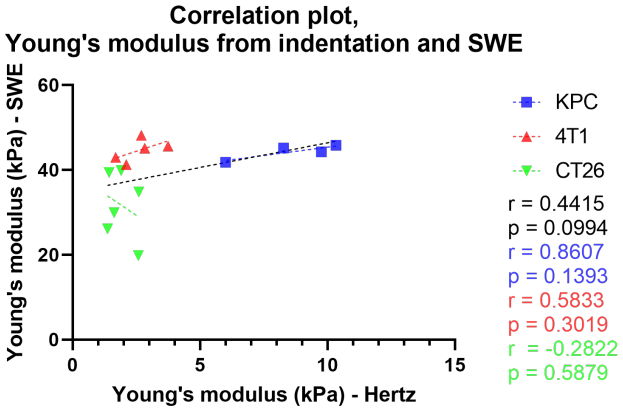

(c)

Figure 4.6.2: Scatter plot showing the correlation between spring constant and Young's modulus from indentation (a), spring constant and Young's modulus from SWE (b), and Young's modulus from indentation and SWE (c). Each data point represents the average measured parameter per tumor. The individual regression lines are calculated from data points originating from the same tumor model, and the black line is a linear regression line for all data points. The Pearson r and p values are included in the lower right corners of all plots. Statistically significant regression lines are solid, and regression lines lacking statistical significance are dashed.

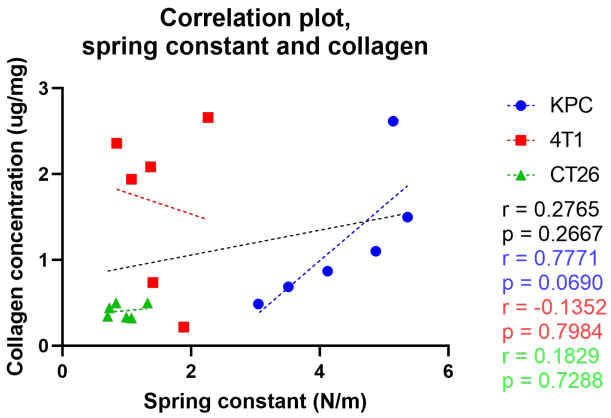

(a)

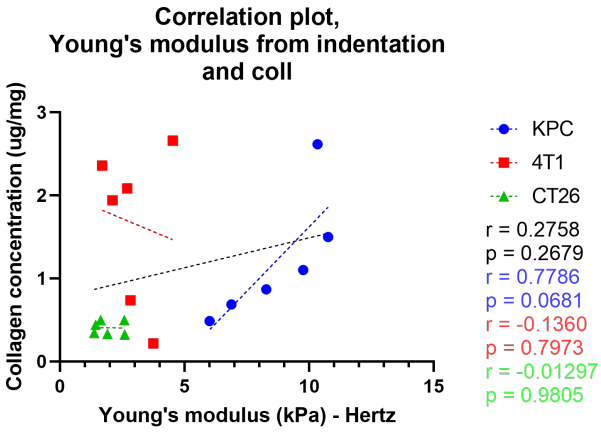

(b)

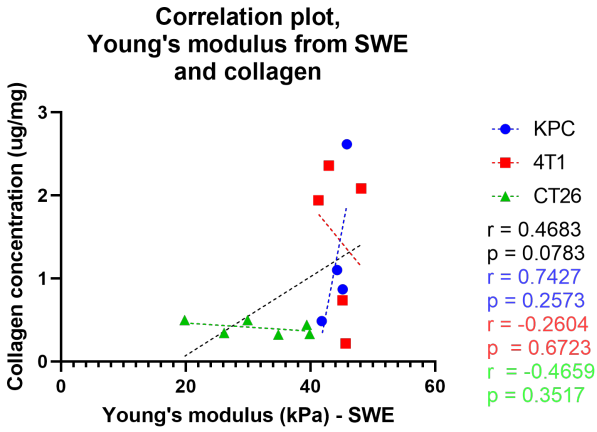

(c)

Figure 4.6.3: Scatter plot showing the correlation between collagen concentration and spring constant (a), Young's modulus from indentation (b), and Young's modulus from SWE (c). Each data point represents the average collagen concentration, and average measured parameter per tumor. The individual regression lines are calculated from data points originating from the same tumor model, and the black line is a linear regression line for all data points. The Pearson r and p values are included in the lower right corners of all plots. Statistically significant regression lines are solid, and regression lines lacking statistical significance are dashed.

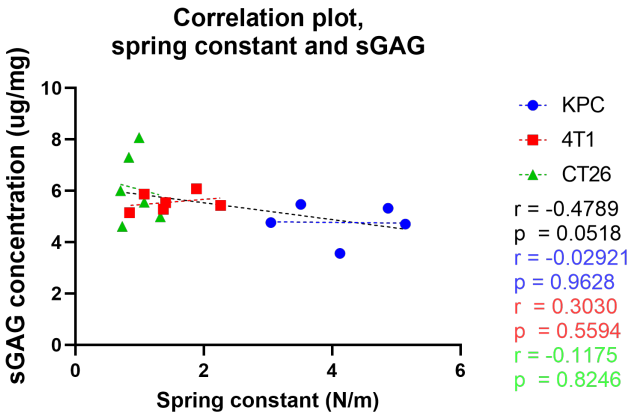

(a)

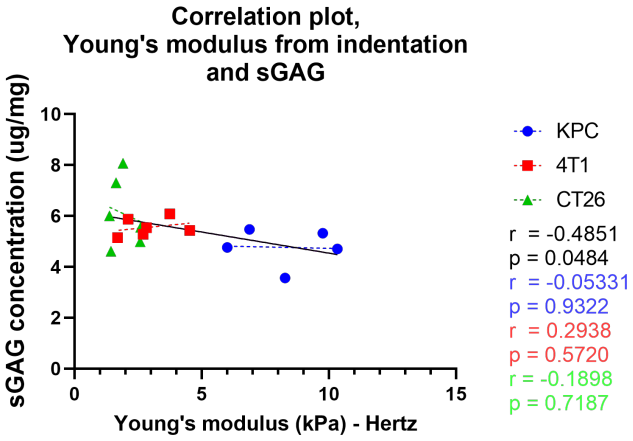

(b)

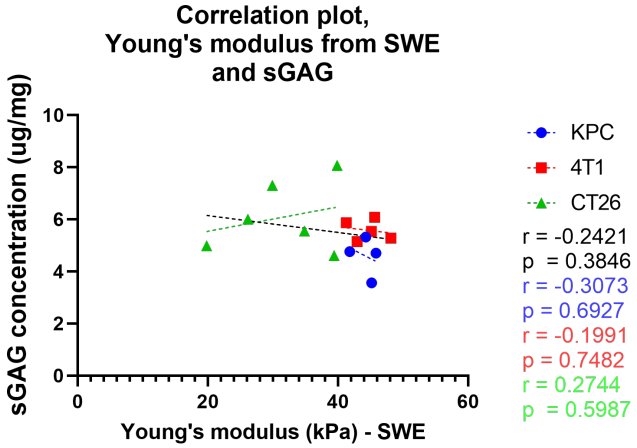

(c)

Figure 4.6.4: Scatter plot showing the correlation between sGAG concentration and spring constant (a), Young's modulus from indentation (b), and Young's modulus from SWE (c). Each data point represents the average sGAG concentration, and average measured parameter per tumor. The individual regression lines are calculated from data points originating from the same tumor model, and the black line is a linear regression line for all data points. The Pearson r and p values are included in the lower right corners of all plots. Statistically significant regression lines are solid, and regression lines lacking statistical significance are dashed.

4.6.3 Correlation between collagen and sGAG concentration

Figure 4.6.5 shows the scatter plots of collagen and sGAG concentrations. The data points represents mean values for each tumor. A linear regression line for all data points and for individual tumor models is included. There is a small negative correlation between collagen and sGAG contents. Individually there is no correlation for KPC, a large negative correlation for 4T1, and a small negative correlation for CT26. However, none of the correlations are statistically significant correlation.

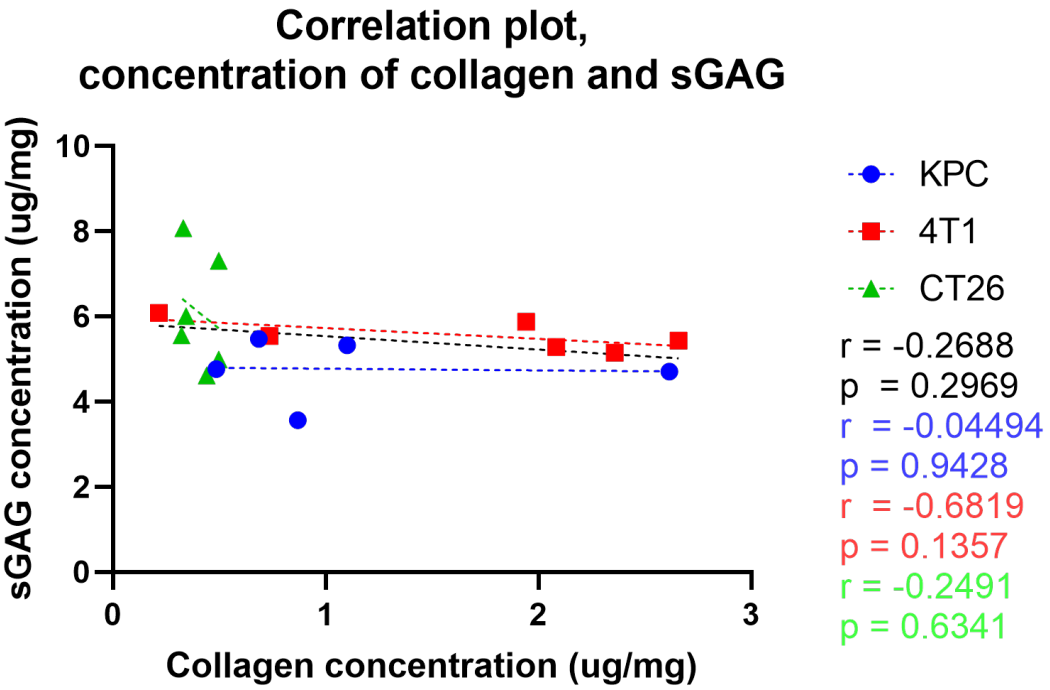

Figure 4.6.5: Scatter plot showing the correlation between collagen and sGAG concentration. Each data point represents the average collagen and sGAG concentration per tumor. The individual regression lines are calculated from data points originating from the same tumor model, and the black line is a linear regression line for all data points. The Pearson r and p values are included in the lower right corners of all plots. Statistically significant regression lines are solid, and regression lines lacking statistical significance are dashed.

4.6.4 Correlation between experimental measurements and tumor weight

Figure 4.6.6 show the scatter plots of weight and all experimental measurements, i.e. spring constant, Young's modulus, and concentrations of sGAG and collagen. Linear regression lines for all data points and for individual tumor models are included. Plots for indentation data show a strong negative correlation between spring constant and weight, and Young's modulus and weight. These results are

statistically significant, as $p < 0.0001$. Individually, there are negative correlations between stiffness measurements and weights, however these are not statistical significant. Figure 4.6.6c show a large positive correlation between Young's modulus and weight for KPC and CT26, and a small negative correlation for 4T1. The correlation for CT26 is statistically significant ($r = 0.8410$, $p = 0.0359$). Regression line for all data points shows $r \approx 0$, i.e. no correlation. Figure 4.6.6d show a medium positive correlation between weight and collagen concentration for KPC and 4T1, and a medium negative correlation for CT26. However, none of the correlations are statistically significant, and the regression line for all data points show no correlation. In Figure 4.6.6e there is a large negative correlation between sGAG concentration and weight for KPC and 4T1, and a small positive correlation for CT26. The regression line for all data points show a medium positive correlation. However, none of these results are statistically significant.

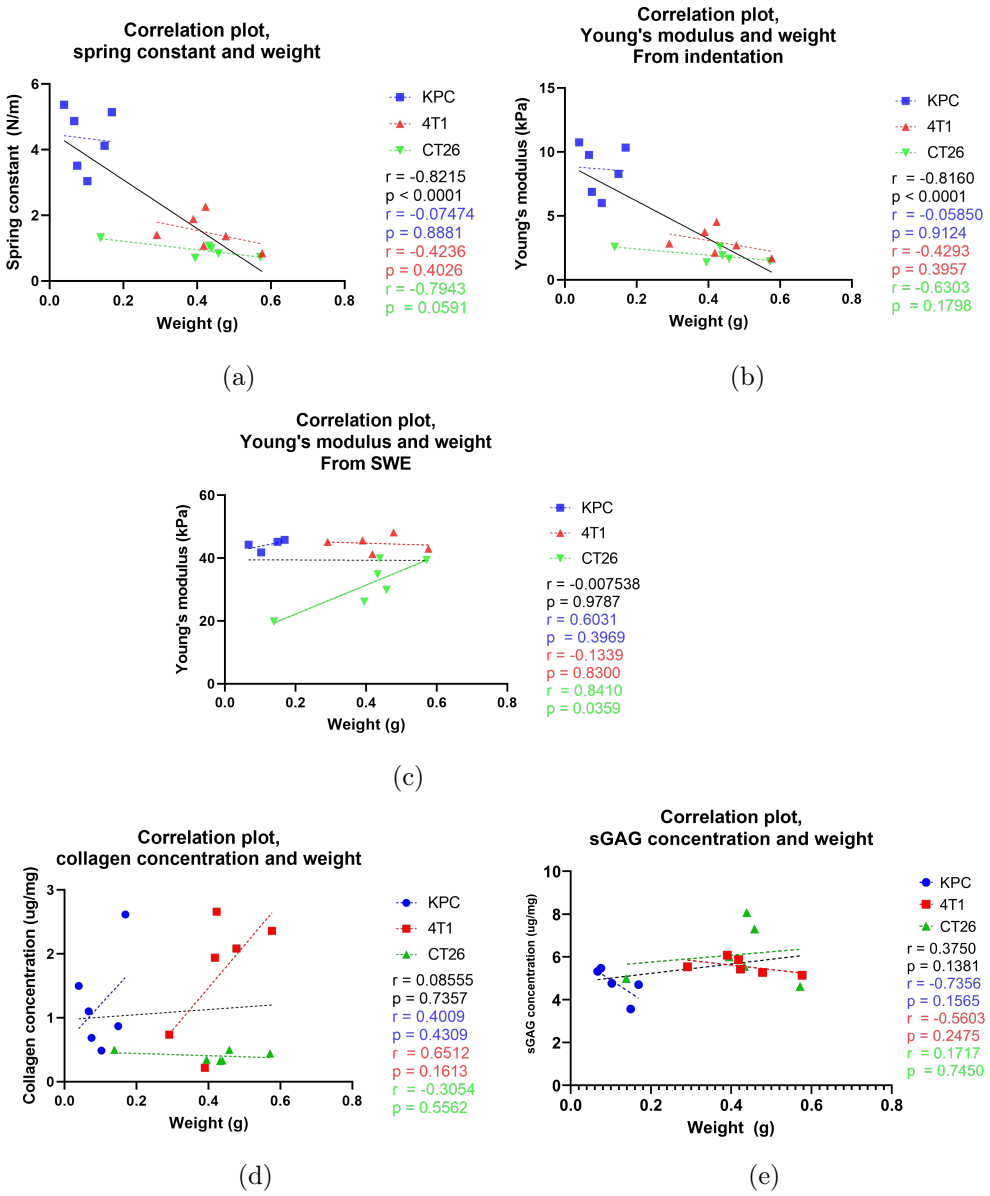

Figure 4.6.6: Scatter plot showing the correlation between weight and spring constant (a), weight and Young's modulus from indentation (b), weight and Young's modulus from SWE (c), weight and collagen concentration (d), and weight and sGAG concentration (e). Each data point represents the weight in grams, and average measured parameter per tumor. The individual regression lines are calculated from data points originating from the same tumor model, and the black line is a linear regression line for all data points. The Pearson r and p values are included in the lower right corners of all plots. Statistically significant regression lines are solid, and regression lines lacking statistical significance are dashed. (a) and (b) show a statistical significant large negative correlation between weight and spring constant, and weight and Young's modulus, respectively. No other results were statistically significant.

4.7 Inter- versus intraheterogeneity

Table 4.7.1 presents the proportion of intraheterogeneity relative to the total heterogeneity (f), as introduced in Equation 2.8. f is calculated for all results, i.e. from indendtaion, shear wave elastography, and collagen and sGAG assays. Intraheterogeneity was calulated from measurements originating from the same tumor, whilst interheterogeneity was calculated from all measurements from the same tumor model.

The results from all data sets show that the interheterogeneity is the dominating factor, with exception for sGAG data for 4T1. However, for some data sets, the factor f is almost equal to 0.5, which indicates that there is almost an equal contribution from both inter- and intraheterogeneity. This applies for the spring constant, Young's modulus (Hertz), and collagen concentration for CT26, and Young's modulus (SWE) and sGAG concentration for KPC. The calculated intra- and interheterogeneity is found in Appendix F in Table F.1.

Table 4.7.1: The proportion of intraheterogeneity relative to the total heterogeneity (f), calculated for data from SWE, indentation, and collagen and sGAG assays.

Tumor type	f
Spring constant	
KPC	0.346
4T1	0.419
CT26	0.468
Young's modulus (Hertz)	
KPC	0.334
4T1	0.417
CT26	0.483
Young's modulus (SWE)	
KPC	0.475
4T1	0.353
CT26	0.237
Collagen concentration	
KPC	0.400
4T1	0.333
CT26	0.462
sGAG concentration	
KPC	0.483
4T1	0.617
CT26	0.334

CHAPTER

FIVE

DISCUSSION

5.1 Force curves and curve fitting

The majority of force curves obtained from indentation with KPC and 4T1 had the same shape; exponential rise the first 100 μm, and an almost linear relation between force and indentation depth the last 100 μm. A study performed by Efremov et al. (2020) showed that the shape of the force-indentation curve is dictated by the underlying viscoelastic relaxation function [56]. The shape of the force-indentation curves for KPC and 4T1 corresponds to the curves presented by Efremov et al., which indicates that these tumor models are viscoelastic. This is according to our knowledge about the material characteristics of tumor tissue, and biological tissue in general. The force curve obtained from indentation with CT26 tumors showed a linear relation between force and indentation depth, indicating different material characteristics. The differences in material characteristics could be further examined by looking at the relaxation and retraction curve from indentation experiments; these were not logged in this project.

The shape of the curves dictated which model had the best curve fit. Hertz model showed a better fit to the force curves for KPC and 4T1, and the linear Hooke's law showed a better fit to the force curves for CT26. This was also reflected in the R^2 values, where high R^2-values indicate good fit of the models [54]. However, additional high p-values suggest suggest a lack of statistical significance for the predictor variable, i.e. the spring constants and Young's modulus.

5.2 Stiffness measurements

Young's modulus

In this project, Young's modulus was estimated using indentation and shear wave elastography. The indentation data showed KPC having a significantly higher Young's modulus than both 4T1 and CT26, which were similar. The SWE data showed 4T1 and KPC having equally high values for Young's modulus, which were significantly higher than for CT26.

There was four outliers removed from the SWE data set, which all originated from a 4T1 tumor. Despite having a Young's modulus significantly higher than

for the rest of the population, it is possible that these outliers are valid since they are comparable for all four tumors. However, there are no observations of higher stiffness measurements in the indentation data for the tumor, and thus, these outliers have been removed from the data set. Causes of experimental errors and bad signals in SWE could be caused by high concentrations of collagen, necrosis and poor vascularity, as well as reflection of the ultrasound wave and signal interference. However, the tumors in question did not display high values in the standard deviation image.

There was one outlier removed from the indentation data set, originating from one out of 8 measurements of a CT26 tumor section. Since it was only one measurement it is most likely caused by experimental error. Experimental errors in indentation experiments could be caused by movements disrupting the measurements of the highly sensitive probe. However, due to little noise in the force curve in Appendix D, it is more likely that it is caused by local morphological differences.

The Young's moduli calculated from SWE data were generally much higher than the ones originating from indentation data. Comparing to stiffness measurements of agar phantoms show a consistent tendency of measuring a higher Young's modulus using SWE compared to indentation. Agar phantoms, with its biomechanical properties depending on the agar concentration, are often used to mimic the elastic properties of biological tissues [57]. Song et al. (2014) performed shear wave elastography of agar phantoms, and measured the shear wave velocity of a 2.0 % (m/v) agar phantom to be ~ 7.0 m/s, which corresponds to a Young's modulus of 147 kPa [58]. In comparison, Maccabi et al. (2016) used a muscle motor system to perform indentation on a 2.0 % (m/v) agar phantom, and calculated the Young's modulus from the force indentation curve to be 102.90 kPa [59]. The experimental methods used in these studies are comparable to micro indentation and SWE performed in this project. The differences in Young's moduli reported in the studies are in accordance with the results from micro indentation and SWE in this project.

Rao et al. (2019) measured the stiffness of orthotopic 4T1 tumors using a macroscopic indentation device with a 2 mm cylindrical probe, and found average Young's modulus of ~ 7 kPa [60]. In this project, the average Young's modulus from indentation data was 3.027 for 4T1, which is lower than what Rao et al. found, but within the same order of magnitude. There are some important differences between the experimental set-up; firstly, the probe used by Rao et al. is bigger (2 mm) than the one used in this project (1 mm). Young's modulus is directly related to the square root of the radius in Equation 2.4. Secondly, their choice of indentation speed, which ranged from 0.01 to 40 mm/s, is faster than what is used in this project, 0.002 mm/s. Huth et al. (2019) performed a study looking at the dependence of Young's moduli on indentation speed for a thin polyacrylamide (PAAm) sample using AFM [61]. PAAms are viscoelastic, thus making them comparable to biological tissue. The measurements resulted in higher Young's moduli for higher indentation speeds. These differences could explain why Rao et al. measured a higher Young's modulus than this project. Otherwise, the experimental procedures are comparable.

Nabavizadeh et. al (2020) measured the Young's modulus for KPC tumor models using harmonic motion elastography (HME) *in vivo* [62]. This method was chosen instead of SWE because no SWE studies have distinctly reported the

Young's modulus values for the perilesional regions, i.e. the region located between the tumor and non-neoplastic region non-invasively. In their work, Young's modulus was estimated to be 11.3 ± 1.7 kPa. This is close to the mean result from indentation experiments (8.30 kPa), but much lower than from SWE (44.04 kPa), a method which is closely related to the one used by Nabavizadeh et. al. An important difference between their study and this project, is that HME was performed *in vivo* one week after tumor implantation. Differences in Young's modulus could be caused by the difference in growth time, as tumors are reported to become stiffer over time [63].

Seguin et al. (2017) measured the Young's modulus of CT26 tumors using shear wave elastography, and found mean Young's modulus of about 13.5 kPa after 12 days [64]. Similarly to Nabavizadeh et. al, it was performed *in vivo*. Several studies have shown that post-mortem degradation and lack of blood perfusion may disturb *ex vivo* measurements, causing an overestimation of stiffness parameters [65, 66]. Although measures were taken to prevent tissue degradation, this could be the reason this project estimated a higher Young's modulus compared to similar elastography experiments.

Rao et al.'s study provides validation for the Young's moduli obtained from indentation data in this thesis. Otherwise, there is a significant variability depending on the experimental method used in other studies, which highlights that the Young's modulus cannot be considered as an absolute value. However, in studies comparing tumor stiffness and delivery of drugs, the absolute value of Young's modulus is not needed, but the relative difference between the tumor models.

As mentioned in Section 2.2.3, Hertz model assumes that the indentation depth is limited to 5-10% of the sample thickness [30]. With an indentation depth of 200 μm, the sample should be no thinner than 2-4 mm. In cases of the indentation depth exceeding the assumptions of the model, this would have lead to measuring the mechanical properties of the petri dish in which the tumor was placed. The petri dish, being made of polystyrene, is inherently stiffer than soft biological tissue [39]. Comparing to the measurements of the tumor sizes in Appendix C, these precautions should satisfy the requirements of the model. However, for the larger tumors ($m > 0.2$ g) which were cut in half, this depends on the precision of the cutting.

Another assumption of Hertz model is that the distance from the tip to the sample's edge should be at least ten times the tip radius, i.e. for a tip radius of 0.5 mm, the distance should me at least 5.0 mm [30]. Comparing to the measurements in Appendix C, this would not be fulfilled for the majority of the tumors. These conditions violate the Hertz assumption and lead to an overestimation of Young's modulus [67].

Spring constant

Indentation data showed the KPC tumors inhibited a significantly higher spring constant than both 4T1 and CT26, which were similarly low. There was a significant strong correlation between the indentation data, i.e. spring constants and Young's moduli ($r = 0.9993$, $p < 0.0001$). This is because they are calculated from the same data set. Thus, they exhibit the same trends when compared to other data sets. There are no studies that have measured the spring constant of

tumors, nor any relevant healthy biological tissue, thus the estimates can not be compared to literature.

Hooke's law assumes small forces and deformations, since the stress-strain relationship becomes nonlinear otherwise. In addition, it only applies when the elastic limit is not exceeded. Assuming the same limitations to indentation depths as for Hertz law, there is a possibility that the indentation depths surpassed the limits of Hooke's law. This would have caused an overestimation of the spring constant. When applied to biological tissues, Hooke's law is often used in conjunction with the linear viscous Newtonian Dash-pot, which describes long term shear modulus behavior, to properly examine the viscoelastic properties of biological tissue under spring force and displacement [15]. As Hertz law showed a better goodness of fit to KPC and 4T1, which exhibited visoscelastic characteristics in their force-deformation curves, it could be that Hooke's law on its own is too simple for biological, viscoelastic tissues.

5.3 Concentration of ECM constituents

There was a significantly higher collagen concentration in the 4T1 tumors than in the CT26 tumors. The collagen content of the KPC tumors was comparable to both 4T1 and CT26. There were no statistical significant difference between the sGAG measurements of the tumor models. Consequently, studies of the delivery of therapeutic agents to these three tumor models could potentially identify the contents of collagen as a barrier within the ECM.

Six outliers were removed from the collagen data set, originating from two CT26 tumors. Two outliers originated from the same sample, the four remaining outliers originated from two samples of the same tumor. The outliers are suggested to originate from experimental error. This is because the preparation of the sample consist of many steps which all could contribute to error, with the most critical step being the draining step(s) [49, 48]. The draining step involves a high risk of sample loss, and to avoid this there was sometimes a trade-off so that not every single drop of fluid, containing unbound dye, was removed. However, this was not deemed as critical for the collagen assay, as it involved two draining steps. Nevertheless, it cannot be ruled out that the discrepancy could be a result of biological variation, especially since four of the outliers originate from the same tumor. There were very little variation between the collagen measurements of the CT26 tumors. Additionally, as can be seen in Appendix F, both inter- and intra-heterogeneity were very low, and almost equal to each other. This could indicate that the CT26 tumors overall have a uniform collagen composition throughout the tumor. The outliers, which were higher than the other measurements, could have been caused by local accumulations of collagen, for example near the periphery of the tumor.

Samples for sGAG assays were more prone to experimental error in the draining step [49, 48]. Additionally, the amount of sGAG was smaller (0 - 5 μg) compared to collagen (0 - 50 μg), making loss of sample more critical. However, no outliers were removed from the sGAG data set.

A study perfromed by Baylon et al. (2022) looking at the relation between osmotic swelling responses in cartilage tissue and contents of collagen and sGAG

found a significant large negative correlation between collagen and sGAG concentrations (ρ = -0.874, p < 0.0001) [68]. In this study, 4T1 and CT26 exhibited a negative trend between collagen and sGAG contents, but not a statistically significant correlation. However, Baylon et al. performed studies on healthy tissue, which is not comparable to tumor tissue. There are no published study correlating the concentrations in tumor tissue.

Davis et al. (2001) characterized the concentrations of collagen and sGAG in s.c. and orthotopic human osteosarcoma OHS tumors grown in mice, using colorimetry [69]. The s.c. osteosarcomas, which are most comparable to the tumors used in this study, contained 1.57 and 0.44 μg/mg wet tissue collagen and sGAG, respectively. The collagen concentrations are comparable to the results in this thesis, with the exception of CT26, which contained 0.41 μg sGAG per mg tumor. The sGAG concentrations found by Davies et al. are about ten times lower then that was found in the 4T1, KPC, and CT26 tumors in this thesis. The following year, Davies et al. performed a similar project using s.c. rat rhabdomyosarcoma [70]. They estimated the collagen and sGAG concentrations to be 4.4 - 6.8 and 0.3 - 0.4 μg/mg wet tissue, respectively. The estimations of collagen concentrations are higher than in this thesis, but comparable and within the same order of magnitude. The experimental methods used in Davies et a.'s study is comparable to the ones employed in this study, and thus the differences between the measurements is mainly attributed to differences between the tumor models.

In a study performed by Netti et al. (2000) they measured the collagen and sGAG concentrations in four tumor models: human colon adenocarcinoma LS174T, human glioblastoma U87, human soft tissue sarcoma HSTS 26T and murine mammary carcinoma MCalIV [6]. All tumor models were implanted s.c. in the leg. They estimated collagen and sGAG concentrations within the range 2 - 8.8 and 0.10 - 0.16 μg/mg wet tissue, respectively. Compared to Davies et al.'s findings, the collagen range is higher, but the sGAG range is lower. However, the values are comparable and in the same order of magnitude. The methods used in Netti's characterization are the same as Davies'. Since the methods are the same, the differences are most probably caused by differences between tumor models.

All three studies have performed colorimetric assays for determining collagen and/or sGAG contents, and have comparable results among themselves. The estimates for collagen concentrations were comparable to those found in this project as well. However, the sGAG concentrations were about ten times lower then that was found in the 4T1, KPC, and CT26 tumors in this thesis. Hence, the findings of this project may possess some uncertainty when it comes to determining the absolute concentrations for the tumor models. Nevertheless, these findings appear plausible considering the lack of existing literature measuring the collagen and/or sGAG content specifically for our three tumor models.

All three studies have performed colorimetric assays for determining collagen and/or sGAG contents of different tumor models, and have comparable results among themselves. Differences between their results and the results from this study is mainly caused by biological differences between the tumor models. The estimates for collagen concentrations were comparable to those found in this project as well. Small differences

However, the sGAG concentrations were about ten times lower then that was found in the 4T1, KPC, and CT26 tumors in this thesis. Hence, the findings

of this project may possess some uncertainty when it comes to determining the absolute concentrations for the tumor models. Nevertheless, these findings appear plausible considering the lack of existing literature measuring the collagen and/or sGAG content specifically for our three tumor models.

The majority of the tumors used in the studies mentioned originate from humans, while this project used murine tumors. There are differences between human and murine tumors that could have contributed to the gap between the measurements and the literature. For instance, murine tumors are reported to typically be more homogeneous than human tumors [71].

5.4 Association between tumor stiffness and collagen and sGAG concentrations

Correlation analysis between stiffness measurements and collagen concentration obtained in this study showed a large positive correlation only for KPC, which was the stiffest tumor model. For the most part, the other tumor models showed a negative relationship between the two parameters. Literature on the subject recognizes increased collagen density as a major contribution to increased tumor stiffness [5, 72]. Calò et al. (2020) performed spatial mapping of the collagen distribution in human liver samples, obtained from colon cancer patients, using AFM [73]. In the study they found a positive correlation between the elastic modulus of the tissue and the collagen content ($r = 0.33$, $P < 0.0001$).

One can speculate that the stiffness of the tumors must surpass a certain level for there to be a positive correlation between the two parameters. Additionally, it rises the question of which other factors could cause variations in tumor stiffness. In addition to the accumulation of ECM constituents, mainly collagen and hyaluronan, tissue stiffening is caused by an increase in the amount of cancer and stromal cells. Variations in the amount of HA, and cancer and stromal cells could have caused the deviation from results reported in litterature.

GAGs have water binding properties due to their anionic characteristics [14]. Bound water acts as a plasticizer of biological tissues, meaning that an increase in bound water contents results in an decrease in the tissue stiffness [74]. One could assume that tumors containing larger amounts of sGAG also contained larger amounts of bound water, making them softer than the tumors containing less sGAG. This would explain the negative non-significant trend between sGAG and stiffness measurements.

5.5 Tumor mass

The indentation data showed a significant decreasing stiffness with increasing weight. There were some differences between the tumor masses, both within the tumor models and between them. The KPC tumors, which also were the stiffest, were the smallest, while CT26 and 4T1 were bigger and similar to each other. It is known that necrosis, along with hypoxia, is more commonly observed in solid tumors when they have exceeded 4 mm in diameter [75]. Necrotic areas have lower stiffness values compared with solid tumor components [76]. In addition to

being of similar size, the indentation data yielded similar stiffness parameters for 4T1 and CT26. Higher levels of necrosis in these tumors could have caused the negative correlations between tumor size and stiffness.

The SWE data showed a positive correlation between Young's modulus and weight for CT26 ($r = 0.8410$, $p = 0.0359$). There was a positive trend between Young's modulus and weight for KPC, and a small negative trend for 4T1, however these were not statistically significant. Several studies have reported a positive correlation between stiffness parameters and mass. For instance, Chamming's et al. (2013) looked at the elasticity of a human tumor xenograft tumor model HBCx3 *in vivo*, using shear wave elastography during tumor growth [77]. The stiffness increased as the tumor grew, showing a strong correlation between size and stiffness ($r = 0.94$, $p < 0.0001$). In this study, the tumors originating to the same tumor model were implanted and harvested at the same time, meaning intertumor differences in size were caused by other factors.

Nia et al. found no correlation between tumor size and stiffness in a study from 2017 [78]. They measured the stiffness of MMTV-M3C breast tumors using AFM. This could indicate that the negative correlations found between indentation data and tumor weights are highly dependent on the tumor model. On the other hand, the differences in the trends between the indentation data and weight, and SWE data and weight, could also indicate that the trends seen here are only coincidental.

Other studies have looked at the relation between stiffness measurements and tumor volume, which is comparable to tumor mass. Hadjigeorgiou et al. (2023) measured the stiffness and tumor volume of 4T1 tumors, and found a significant positive, nonlinear correlation ($\rho = 0.84$, $p = 0.0025$) [79]. The results from the study performed by Seguin et al. also showed a positive correlation between the volume of CT26 tumor models and their shear modulus parameter ($r = 0.59$, $p < 0.0001$), which is linearly related to Young's modulus [64]. The correlation between tumor size and stiffness parameters could be further examined by looking at tumor volume, or by examining possible non-linear correlations. For instance the equation used by Hadjigeorgiou et al. for curve fitting in their correlation analysis: $E = k_1 - k_2 e^{-k_3 V}$, where E is the elastic modulus, V the tumor volume and k_1, k_2, and k_3 are the fitted parameters [79].

There was an increasing collagen concentration for increasing weight for KPC and 4T1 tumors, and a decreasing sGAG concentration. For CT26, there was a negative trend between collagen content and weight, and a positive trend between sGAG content and weight. However, all correlation plots lack statistical significance. Davies et al.'s study from 2001 found a significant positive correlation between collagen and tumor volume in the s.c. osteosarcoma, and a negative correlation for the orthotopic osteosarcoma [69]. There was also a significant positive correlation between sGAG contents and tumor volume for the orthotopic osteosarcoma. The implantation site is known to cause differences in morphologic and metabolic patterns [80].

5.6 Tumor heterogeneity

The complexity of tumors causes large variations within and between tumor models, which has been observed in this project. Calculations of the inter- versus in-

traheterogeneity indicate that these variations mainly stem from variations within the tumor family, i.e. the intertumor heterogeneity. However, the intraheterogeneity is relatively high, especially for indentation, collagen and sGAG data. High intratumor heterogeneity stems from a heterogeneous cell population, and has been observed in a several different cancer types, including breast tumors [81]. For the indentation data, the large intratumor variation is very dependent on the positions of the measurements. The contact diameter of a probe is given by the equation $R_c = 2\sqrt{R\delta - \frac{\delta}{4}}$ [39]. Given a probe with a radius $R = 0.5$ mm and an average indentation depth $\delta = 200\mu$m, this results in a contact diameter of 0.45 mm. Collagen fibers can be up to 20 μm in diameter, and the cancer cell lines used in this project range from 10 to 20 μm in diameter [82, 83, 84]. Large intratumor variation of the distribution of these components could cause large differences in stiffness measurements between positions. For the collagen and sGAG data, the choice of tumor pieces during homogenization could cause large variations between the measurements. As mentioned, sGAG and collagen tend to accumulate in the centre and at the periphery, respectively. A random selection of pieces originating from the centre would yield a much higher concentration of sGAG than if the pieces originated from the periphery. Large intravariation of collagen has been proved to worsen prognoses and cause a higher resistance to therapeutics [85]. Thus, delivery studies of therapeutic agents to these three tumor models could be able to identify the impact of collagen intraheterogeneity.

5.7 Future work

In Section 5.2 results from similar projects were presented, the majority of which performed stiffness measurements of tumors *in vivo*. Performing *in vivo* measurements enables investigation of the development of tumor stiffness over time. This would also eliminate the effects of post-mortem degradation, which could have lead to overestimation of the stiffness measurements in this thesis. To be able to perform SWE *in vivo* one would need a ultrasound prove fitting to small tumors in mice. Additional improvements of the SWE technology could yield more precises measurements of shear wave velocity.

Future work should also use a uniform tumor size distribution. Studies have shown that the amount of collagen is positively correlated to the size of the tumor [86]. There were some differences between the sizes of the tumors used in this project, both within the same tumor model and between them, which could have affected the correlation analysis of stiffness measurements vs. concentrations of collagen and sGAG.

CHAPTER

SIX

CONCLUSIONS

The aim of this project was to determine the association between tumor tissue stiffness and collagen and sGAG for KPC, 4T1 and CT26 tumor models. The estimated Young's moduli and spring constants were significantly higher for KPC than for CT26, while the stiffness parameters for 4T1 varied depending on the experimental method. CT26 contained significantly less collagen than 4T1, while KPC was comparable to both tumor models. For collagen measurements of KPC and CT26, the contribution of intraheterogeneity relative to the total heterogeneity was high. Consequently, delivery studies of therapeutic agents to these three tumor models might identify the contents of collagen as a potential barrier within the ECM, and identify the impact of collagen intraheterogeneity. No statistically significant differences were observed between the sGAG measurements of the tumor models.

Compared to stiffness estimates in literature, the Young's modulus measured by micro indentation is comparable to results from similar indention experiments. For SWE, this project's findings were higher, which could be explained by post-mortem degradation. To avoid this, future studies should aim to perform measurements *in vivo*, which also will make it possible to study the tumor stiffness over time.

The Young's modulus estimated from SWE was significantly higher than from indentation, which is a consistent trend observed in other projects using same experimental procedures. This highlights that Young's modulus cannot be considered an absolute value, but rather something that depends on the experimental method used. However, in studies comparing tumor stiffness and delivery of drugs, the absolute value of Young's modulus is not needed, but the relative difference between tumor models.

The collagen concentrations measured in this project is comparable to literature, while the concentrations of sGAG were up to tenfold higher. The differences is mainly caused by variations between tumor models. Overall, there was a positive trend between stiffness and collagen concentration, and a negative trend between stiffness and sGAG concentration. However, these were not statistically significant. To further investigate this relation, further studies should use tumors of the same size to avoid the effects of the size dependency of collagen concentrations. There was a negative correlation between the stiffness measurements from indentation and weight, which could have been caused by necrosis. CT26 showed a

positive correlation between Young's modulus from SWE and weight, which is in accordance with literature.

Stiffness and collagen content are important biomarkers for which tumors will have a successful delivery of therapeutics. Hopefully, this project has laid down some of the ground work for future research on the therapeutic consequences of the morphological and physiological differences between tumor models.

REFERENCES

[1] World Health Organization. *Cancer Today*. https://gco.iarc.fr/today/home. Accessed: [03.07.2023]. 2020.

[2] Xiuxiu He, Byoungkoo Lee, and Yi Jiang. In: *Medical Review* 2.2 (2022), pp. 125–139. DOI: doi:10.1515/mr-2021-0028. URL: https://doi.org/10.1515/mr-2021-0028.

[3] Masoud Najafi, Bagher Farhood, and Keywan Mortezaee. "Extracellular Matrix (ECM) Stiffness and Degradation as Cancer Drivers". In: *J Cell Biochem* 120.3, 30321449 (Mar. 2019), pp. 2782–2790. DOI: 10.1002/jcb.27681. URL: https://doi.org/10.1002/jcb.27681.

[4] Maria Kalli and Triantafyllos Stylianopoulos. "Defining the Role of Solid Stress and Matrix Stiffness in Cancer Cell Proliferation and Metastasis". In: *Frontiers in Oncology* 8 (Mar. 2018). DOI: 10.3389/fonc.2018.00055.

[5] Sofie Snipstad et al. "Ultrasound and microbubbles to beat barriers in tumors: Improving delivery of nanomedicine". In: *Advanced Drug Delivery Reviews* 177 (2021), p. 113847. ISSN: 0169-409X. DOI: https://doi.org/10.1016/j.addr.2021.113847. URL: https://www.sciencedirect.com/science/article/pii/S0169409X21002398.

[6] Paolo A. Netti et al. "Role of Extracellular Matrix Assembly in Interstitial Transport in Solid Tumors". In: *Cancer Res* 60.9 (May 2000), pp. 2497–2503.

[7] Radhika M. Bavle. "Mitosis at a glance". In: *Journal of Oral and Maxillofacial Pathology* 18.Suppl 1 (Sept. 2014), S2–S5. DOI: 10.4103/0973-029X.141175.

[8] J. Hardin, G.P. Bertoni, and L.J. Kleinsmith. *Becker's World of the Cell, Global Edition*. Pearson Education, 2017. ISBN: 9781292177779. URL: https://books.google.no/books?id=Lg6lDgAAQBAJ.

[9] Douglas Hanahan and Robert A. Weinberg. "Hallmarks of cancer: the next generation". In: *Cell* 144.5 (2011), pp. 646–674. DOI: 10.1016/j.cell.2011.02.013.

[10] Triantafyllos Stylianopoulos, Lance L. Munn, and Rakesh K. Jain. "Reengineering the Physical Microenvironment of Tumors to Improve Drug Delivery and Efficacy: From Mathematical Modeling to Bench to Bedside". In: *Trends in Cancer* 4.4 (2018). Special Issue: Physical Sciences in Oncology, pp. 292–319. ISSN: 2405-8033. DOI: https://doi.org/10.1016/j.trecan.2018.

02.005. URL: https://www.sciencedirect.com/science/article/pii/S2405803318300402.

[11] L. Wullkopf et al. "Cancer cells' ability to mechanically adjust to extracellular matrix stiffness correlates with their invasive potential". In: *Mol Biol Cell* 29.20 (Oct. 2018), pp. 2378–2385. DOI: 10.1091/mbc.E18-05-0319.

[12] R. Phillips et al. *Physical Biology of the Cell*. Garland Science, 2013. ISBN: 9780815344506. URL: https://books.google.no/books?id=JnyPZwEACAAJ.

[13] Jarett Casale and Jonathan S Crane. "Biochemistry, Glycosaminoglycans". en. In: *StatPearls*. Treasure Island (FL): StatPearls Publishing, Jan. 2023.

[14] Ryan T. Kendall and Carol A. Feghali-Bostwick. "Fibroblasts in fibrosis: novel roles and mediators". In: *Frontiers in Pharmacology* 5 (2014). ISSN: 1663-9812. DOI: 10.3389/fphar.2014.00123. URL: https://www.frontiersin.org/articles/10.3389/fphar.2014.00123.

[15] Ashkan Maccabi et al. "Quantitative characterization of viscoelastic behavior in tissue-mimicking phantoms and ex vivo animal tissues". In: *PLoS One* 13.1 (2018), e0191919. DOI: 10.1371/journal.pone.0191919.

[16] E.A. Fuller and Kevin Kirby. "Subtalar joint equilibrium and tissue stress approach to biomechanical therapy of the foot and lower extremity". In: *Lower extremity biomechanics: theory and practice* 1 (Jan. 2013), pp. 205–264.

[17] Jiacheng Huang et al. "Extracellular matrix and its therapeutic potential for cancer treatment". en. In: *Signal Transduct Target Therapy* 6.1 (Apr. 2021), p. 153.

[18] S. Ishihara and H. Haga. "Matrix Stiffness Contributes to Cancer Progression by Regulating Transcription Factors". In: *Cancers (Basel)* 14.4 (Feb. 2022), p. 1049. DOI: 10.3390/cancers14041049.

[19] Andreas Stylianou et al. "Nanomechanical properties of solid tumors as treatment monitoring biomarkers". In: *Acta Biomaterialia* 154 (2022), pp. 324–334. ISSN: 1742-7061. DOI: https://doi.org/10.1016/j.actbio.2022.10.021. URL: https://www.sciencedirect.com/science/article/pii/S1742706122006778.

[20] Seiichiro Ishihara and Hisashi Haga. "Matrix Stiffness Contributes to Cancer Progression by Regulating Transcription Factors". In: *Cancers* 14.4 (2022). ISSN: 2072-6694. DOI: 10.3390/cancers14041049. URL: https://www.mdpi.com/2072-6694/14/4/1049.

[21] Raghu Kalluri and Michael Zeisberg. "Fibroblasts in cancer". In: *Nature Reviews Cancer* 6.5 (May 2006), pp. 392–401. ISSN: 1474-1768. DOI: 10.1038/nrc1877. URL: https://doi.org/10.1038/nrc1877.

[22] Marie-Louise Thorseth et al. "Uncovering mediators of collagen degradation in the tumor microenvironment". In: *Matrix Biology Plus* 13 (2022), p. 100101. ISSN: 2590-0285. DOI: https://doi.org/10.1016/j.mbplus.2022.100101. URL: https://www.sciencedirect.com/science/article/pii/S2590028522000011.

[23] Nuh N Rahbari et al. "Anti-VEGF therapy induces ECM remodeling and mechanical barriers to therapy in colorectal cancer liver metastases". en. In: *Sci Transl Med* 8.360 (Oct. 2016), 360ra135.

[24] Soo-Hyun Kim, Jeremy Turnbull, and Scott Guimond. "Extracellular matrix and cell signalling: The dynamic cooperation of integrin, proteoglycan and growth factor receptor". In: *The Journal of endocrinology* 209 (Feb. 2011), pp. 139–51. DOI: 10.1530/JOE-10-0377.

[25] Kandice R. Levental et al. "Matrix Crosslinking Forces Tumor Progression by Enhancing Integrin Signaling". In: *Cell* 139.5 (Nov. 2009), pp. 891–906. ISSN: 0092-8674. DOI: 10.1016/j.cell.2009.10.027. URL: https://cir.nii.ac.jp/crid/1362825894571117952.

[26] Rachel Shi, Chengheng Liao, and Qing Zhang. "Hypoxia-Driven Effects in Cancer: Characterization, Mechanisms, and Therapeutic Implications". In: *Cells* 10.3 (2021). ISSN: 2073-4409. DOI: 10.3390/cells10030678. URL: https://www.mdpi.com/2073-4409/10/3/678.

[27] C. Dorado Cortez et al. "Ultrasound shear wave velocity in skeletal muscle: A reproducibility study". In: *Diagnostic and Interventional Imaging* 97.1 (2016), pp. 71–79. ISSN: 2211-5684. DOI: https://doi.org/10.1016/j.diii.2015.05.010. URL: https://www.sciencedirect.com/science/article/pii/S2211568415002077.

[28] *Stress, Strain and Young's Modulus*. Engineeringtoolbox.com, 2019. URL: https://www.engineeringtoolbox.com/stress-strain-d_950.html.

[29] H.D. Young and R.A. Freedman. *University Physics with Modern Physics, Global Edition*. Pearson Education, 2019. ISBN: 9781292314815. URL: https://books.google.no/books?id=b76GEAAAQBAJ.

[30] Stylianos-Vasileios Kontomaris. "The Hertz Model in AFM Nanoindentation Experiments: Applications in Biological Samples and Biomaterials". In: *Micro and Nanosystems* 10 (Apr. 2018). DOI: 10.2174/\\1876402910666180426114700.

[31] Mihra S Taljanovic et al. "Shear-Wave Elastography: Basic Physics and Musculoskeletal Applications". en. In: *Radiographics* 37.3 (May 2017), pp. 855–870.

[32] Jean-Luc Gennisson et al. "Ultrasound elastography: principles and techniques". In: *Diagn Interv Imaging* 94.5 (May 2013), pp. 487–495. ISSN: 2211-5684. DOI: 10.1016/j.diii.2013.01.022. URL: https://doi.org/10.1016/j.diii.2013.01.022.

[33] Kathryn Nightingale, Stephen McAleavey, and Gregg Trahey. "Shear-wave generation using acoustic radiation force: in vivo and ex vivo results". en. In: *Ultrasound Med Biol* 29.12 (Dec. 2003), pp. 1715–1723.

[34] Russell Goodall and Andreas Mortensen. "24 - Porous Metals". In: *Physical Metallurgy (Fifth Edition)*. Ed. by David E. Laughlin and Kazuhiro Hono. Fifth Edition. Oxford: Elsevier, 2014, pp. 2399–2595. ISBN: 978-0-444-53770-6. DOI: https://doi.org/10.1016/B978-0-444-53770-6.00024-1. URL: https://www.sciencedirect.com/science/article/pii/B9780444537706000241.

[35] Bin Liu, Zhang Lixian, and Huajian Gao. "Poisson ratio can play a crucial role in mechanical properties of biocomposites". In: *Mechanics of Materials - MECH MATER* 38 (Dec. 2006), pp. 1128–1142. DOI: 10.1016/j.mechmat.2006.02.002.

[36] JeongAh Ryu and Woo Jeong. "Current status of musculoskeletal application of shear wave elastography". In: *Ultrasonography* 36 (Feb. 2017). DOI: 10.14366/usg.16053.

[37] Andrey Orekhov. "Statistical criteria for the limits of application of Hooke's law". In: *Vestnik of Saint Petersburg University. Applied Mathematics. Computer Science. Control Processes* 16 (Jan. 2020), pp. 391–401. DOI: 10.21638/11701/spbu10.2020.404.

[38] Emilios K. Dimitriadis et al. "Determination of Elastic Moduli of Thin Layers of Soft Material Using the Atomic Force Microscope". In: *Biophysical Journal* 82.5 (2002), pp. 2798–2810. ISSN: 0006-3495. DOI: https://doi.org/10.1016/S0006-3495(02)75620-8. URL: https://www.sciencedirect.com/science/article/pii/S0006349502756208.

[39] S V Kontomaris and A Malamou. "Hertz model or Oliver amp; Pharr analysis? Tutorial regarding AFM nanoindentation experiments on biological samples". In: *Materials Research Express* 7.3 (Mar. 2020), p. 033001. DOI: 10.1088/2053-1591/ab79ce. URL: https://dx.doi.org/10.1088/2053-1591/ab79ce.

[40] Yuri M. Efremov et al. "Measuring nanoscale viscoelastic parameters of cells directly from AFM force-displacement curves". In: *Scientific Reports* 7.1 (May 2017), p. 1541. ISSN: 2045-2322. DOI: 10.1038/s41598-017-01784-3. URL: https://doi.org/10.1038/s41598-017-01784-3.

[41] J.T. Cheung and M. Zhang. "7 - Mechanics of the human skin and underlying soft tissues". In: *Biomechanical Engineering of Textiles and Clothing*. Ed. by Y. Li and X.-Q. Dai. Woodhead Publishing Series in Textiles. Woodhead Publishing, 2006, pp. 111–124. ISBN: 978-1-84569-052-6. DOI: https://doi.org/10.1533/9781845691486.2.111. URL: https://www.sciencedirect.com/science/article/pii/B9781845690526500078.

[42] Andrea Rubiano, Cameron Galitz, and Craig S. Simmons. "Mechanical Characterization by Mesoscale Indentation: Advantages and Pitfalls for Tissue and Scaffolds". In: *Tissue Engineering Part C: Methods* 25.10 (Oct. 2019), pp. 619–629. ISSN: 1937-3392. DOI: 10.1089/ten.TEC.2018.0372. eprint: 2019May15. URL: https://doi.org/10.1089/ten.TEC.2018.0372.

[43] Maxwell C McCabe et al. "Evaluation and Refinement of Sample Preparation Methods for Extracellular Matrix Proteome Coverage". en. In: *Mol Cell Proteomics* 20 (June 2021), p. 100079.

[44] Rakesh Heda, Felipe Toro, and Charles R. Tombazzi. *Physiology, Pepsin*. [Updated 2022 May 8]. In: StatPearls [Internet]. Treasure Island (FL): StatPearls Publishing; Jan. 2023. URL: https://www.ncbi.nlm.nih.gov/books/NBK537005/.

[45] Fang Yu et al. "Optimization of Extraction Conditions and Characterization of Pepsin-Solubilised Collagen from Skin of Giant Croaker (Nibea japonica)". In: *Marine Drugs* 16.1 (Jan. 2018), p. 29. ISSN: 1660-3397. DOI: 10.3390/md16010029. URL: https://www.ncbi.nlm.nih.gov/pmc/articles/PMC5793077/.

[46] Young-Min Kang et al. "Papain Ameliorates Lipid Accumulation and Inflammation in High-Fat Diet-Induced Obesity Mice and 3T3-L1 Adipocytes via AMPK Activation". In: *International Journal of Molecular Sciences* 22.18 (Sept. 2021), p. 9885. ISSN: 1661-6596. DOI: 10.3390/ijms22189885. URL: https://www.ncbi.nlm.nih.gov/pmc/articles/PMC8468764/.

[47] A.J. Barrett, N.D. Rawlings, and J.F. Woessner. *Handbook of Proteolytic Enzymes*. Handbook of Proteolytic Enzymes, Two-Volume Set with CD-ROM. Elsevier Science, 2012. ISBN: 9780123822208. URL: https://books.google.no/books?id=XBuHJLFRjRkC.

[48] Biocolor Ltd. *Sircol™ - Soluble Collagen Assay Kit*. https://www.biocolor.co.uk/ecm-assays/sircol-soluble-collagen-assay. Visited on May 29th 2023. 2022.

[49] Biocolor Ltd. *Blyscan™ - Sulfated Glycosaminoglycan (sGAG) Assay Kit*. https://www.biocolor.co.uk/ecm-assays/blyscan-glycosaminoglycanassay. Visited on May 29th 2023. 2022.

[50] Joshua M. Pearce. "Chapter 6 - Digital Designs and Scientific Hardware". In: *Open-Source Lab*. Ed. by Joshua M. Pearce. Boston: Elsevier, 2014, pp. 165–252. ISBN: 978-0-12-410462-4. DOI: https://doi.org/10.1016/B978-0-12-410462-4.00006-8. URL: https://www.sciencedirect.com/science/article/pii/B9780124104624000068.

[51] Ingvil Bjørnæs and Einar K. Rofstad. "Microvascular permeability to macromolecules in human melanoma xenografts assessed by contrast-enhanced MRI — intertumor and intratumor heterogeneity". In: *Magnetic Resonance Imaging* 19.5 (2001), pp. 723–730. ISSN: 0730-725X. DOI: https://doi.org/10.1016/S0730-725X(01)00377-0. URL: https://www.sciencedirect.com/science/article/pii/S0730725X01003770.

[52] Andrew Murphy and Balint Botz. "Pulse repetition frequency". In: Nov. 2018. DOI: 10.53347/rID-64450.

[53] *Image Processing Toolbox*. MathWorks. Retrieved May 31, 2023, from https://se.mathworks.com/products/image.html.

[54] Sal Mangiafico. *Summary and Analysis of Extension Program Evaluation in R*. Jan. 2016.

[55] Harvey J. Motulsky and Ronald E. Brown. "Detecting outliers when fitting data with nonlinear regression – a new method based on robust nonlinear regression and the false discovery rate". In: *BMC Bioinformatics* 7.1 (Mar. 2006), p. 123. ISSN: 1471-2105. DOI: 10.1186/1471-2105-7-123. URL: https://doi.org/10.1186/1471-2105-7-123.

[56] Yu. M. Efremov, S. L. Kotova, and P. S. Timashev. "Viscoelasticity in simple indentation-cycle experiments: a computational study". In: *Scientific Reports* 10.1 (Aug. 2020), p. 13302. ISSN: 2045-2322. DOI: 10.1038/s41598-020-70361-y. URL: https://doi.org/10.1038/s41598-020-70361-y.

[57] Chunhui Li, Zhihong Huang, and Ruikang Wang. "Elastic properties of soft tissue-mimicking phantoms assessed by combined use of laser ultrasonics and low coherence interferometry". In: *Optics express* 19 (May 2011), pp. 10153–63. DOI: 10.1364/OE.19.010153.

[58] Thu-Mai Nguyen et al. "Shear wave elastography method combining phase-sensitive optical coherence tomography and coded acoustic radiation force". In: Sept. 2014, pp. 651–654. DOI: 10.1109/ULTSYM.2014.0160.

[59] A. Maccabi et al. "An examination of the elastic properties of tissue-mimicking phantoms using vibro-acoustography and a muscle motor system". In: *Review of Scientific Instruments* 87.2 (Feb. 2016), p. 024903. ISSN: 0034-6748. DOI: 10.1063/1.4942049. eprint: https://pubs.aip.org/aip/rsi/article-pdf/doi/10.1063/1.4942049/15838548/024903_1_online.pdf. URL: https://doi.org/10.1063/1.4942049.

[60] Shalini Vasudev Rao, Kurt Ingar Draget, and Catherine Taylor Nordgård. "Youngs's modulus of tumour tissue from an in vivo breast cancer model - effect of treatment with guluronate oligosaccharides". In: *41-47* (2019). URL: https://hdl.handle.net/11250/2650605 (visited on 06/24/2023).

[61] Steven Huth, Sandra Sindt, and Christine Selhuber-Unkel. "Automated analysis of soft hydrogel microindentation: Impact of various indentation parameters on the measurement of Young's modulus". In: *PLOS ONE* 14 (Aug. 2019), e0220281. DOI: 10.1371/journal.pone.0220281.

[62] Alireza Nabavizadeh et al. "Noninvasive Young's modulus visualization of fibrosis progression and delineation of pancreatic ductal adenocarcinoma (PDAC) tumors using Harmonic Motion Elastography (HME) in vivo". In: *Theranostics* 10 (Mar. 2020), pp. 4614–4626. DOI: 10.7150/thno.37965.

[63] Catherine Voutouri and Triantafyllos Stylianopoulos. "Accumulation of mechanical forces in tumors is related to hyaluronan content and tissue stiffness". In: *PLoS One* 13.3 (Mar. 2018), e0193801. DOI: 10.1371/journal.pone.0193801.

[64] Johanne Seguin et al. "Evaluation of Antivascular Combretastatin A4 P Efficacy Using Supersonic Shear Imaging Technique of Ectopic Colon Carcinoma CT26". In: *Ultrasound in Medicine Biology* 43.10 (2017), pp. 2352–2361. ISSN: 0301-5629. DOI: https://doi.org/10.1016/j.ultrasmedbio.2017.05.013. URL: https://www.sciencedirect.com/science/article/pii/S0301562917302107.

[65] Nicole L Ramo et al. "Comparison of in vivo and ex vivo viscoelastic behavior of the spinal cord". In: *Acta Biomaterialia* 68 (2018), pp. 78–89. DOI: 10.1016/j.actbio.2017.12.024.

[66] A. Garo and et al. "Towards a Reliable Characterisation of the Mechanical Behaviour of Brain Tissue: The Effects of Post-mortem Time and Sample Preparation". In: *Print* (Jan. 2007), pp. 51–58.

[67] R. Long et al. “Effects of gel thickness on microscopic indentation measurements of gel modulus”. In: *Biophys J* 101.3 (Aug. 2011), pp. 643–650. DOI: 10.1016/j.bpj.2011.06.049.

[68] Eric G Baylon and Marc E Levenston. “Osmotic Swelling Responses Are Conserved Across Cartilaginous Tissues With Varied Sulfated-Glycosaminoglycan Contents”. In: *J Orthop Res* 38.4 (Apr. 2020), pp. 785–792. DOI: 10.1002/jor.24521.

[69] C. de Lange Davies et al. “Uptake of IgG in osteosarcoma correlates inversely with interstitial fluid pressure, but not with interstitial constituents”. In: *Br J Cancer* 85.12 (Dec. 2001), pp. 1968–1977. DOI: 10.1054/bjoc.2001.2180.

[70] Catharina Davies et al. “Comparison of IgG diffusion and extracellular matrix composition in rhabdomyosarcomas grown in mice versus in vitro as spheroids reveals the role of host stromal cells”. In: *British journal of cancer* 86 (June 2002), pp. 1639–44. DOI: 10.1038/sj.bjc.6600270.

[71] Evgeniy B Eruslanov, Sunil Singhal, and Steven M Albelda. “Mouse versus Human Neutrophils in Cancer: A Major Knowledge Gap”. In: *Trends Cancer* 3.2 (Feb. 2017), pp. 149–160. DOI: 10.1016/j.trecan.2016.12.006.

[72] Johannes Riegler et al. “Tumor Elastography and Its Association with Collagen and the Tumor Microenvironment”. In: *Clinical Cancer Research* 24.18 (Sept. 2018), pp. 4455–4467. ISSN: 1078-0432. DOI: 10.1158/1078-0432.CCR-17-3262. eprint: https://aacrjournals.org/clincancerres/article-pdf/24/18/4455/2047454/4455.pdf. URL: https://doi.org/10.1158/1078-0432.CCR-17-3262.

[73] Annalisa Calò et al. “Spatial mapping of the collagen distribution in human and mouse tissues by force volume atomic force microscopy”. In: *Scientific reports* 10 (Sept. 2020), p. 15664. DOI: 10.1038/s41598-020-72564-9.

[74] G Kerch. “Role of Changes in State of Bound Water and Tissue Stiffness in Development of Age-Related Diseases”. In: *Polymers* 12.6 (2020), p. 1362. ISSN: 2073-4360. DOI: 10.3390/polym12061362. eprint: https://www.mdpi.com/2073-4360/12/6/1362/pdf. URL: https://www.mdpi.com/2073-4360/12/6/1362.

[75] PP Yee and W Li. “Tumor necrosis: A synergistic consequence of metabolic stress and inflammation”. In: *Bioessays* 43.7 (2021), e2100029. ISSN: 1521-1878. DOI: 10.1002/bies.202100029. eprint: https://onlinelibrary.wiley.com/doi/epdf/10.1002/bies.202100029. URL: https://onlinelibrary.wiley.com/doi/full/10.1002/bies.202100029.

[76] Jiaxu Liang et al. “Clinical application of Magnetic resonance elastography in hepatocellular carcinoma: from diagnosis to prognosis”. In: *Annals of Hepatology* 28.2 (2023). ISSN: 16652681. DOI: 10.1016/j.aohep.2022.100889. URL: https://www.elsevier.es/en-revista-annals-hepatology-16-articulo-clinical-application-magnetic-resonance-elastography-S1665268122002319.

[77] Frederic Chamming et al. "Shear wave elastography of tumour growth in a human breast cancer model with pathological correlation". In: *European radiology* 23.8 (Aug. 2013), pp. 2079–2086. ISSN: 0938-7994. DOI: 10.1007/s00330-013-2828-8. URL: https://doi.org/10.1007/s00330-013-2828-8.

[78] Hadi Nia et al. "Solid stress and elastic energy as measures of tumour mechanopathology". In: *Nature Biomedical Engineering* 1 (Nov. 2016), p. 0004. DOI: 10.1038/s41551-016-0004.

[79] Andreas G. Hadjigeorgiou and Triantafyllos Stylianopoulos. "Evaluation of growth-induced, mechanical stress in solid tumors and spatial association with extracellular matrix content". In: *Biomechanics and Modeling in Mechanobiology* (May 2023). ISSN: 1617-7940. DOI: 10.1007/s10237-023-01716-3. URL: https://doi.org/10.1007/s10237-023-01716-3.

[80] Wenting Zhang et al. "Comparative Study of Subcutaneous and Orthotopic Mouse Models of Prostate Cancer: Vascular Perfusion, Vasculature Density, Hypoxic Burden and BB2r-Targeting Efficacy". en. In: *Scientific Reports* 9.1 (July 2019), p. 11117. ISSN: 2045-2322. DOI: 10.1038/s41598-019-47308-z. URL: https://doi.org/10.1038/s41598-019-47308-z.

[81] Gulisa Turashvili and Edi Brogi. "Tumor Heterogeneity in Breast Cancer". In: *Frontiers in Medicine* 4 (2017). ISSN: 2296-858X. DOI: 10.3389/fmed.2017.00227. URL: https://www.frontiersin.org/articles/10.3389/fmed.2017.00227.

[82] Babita Shashni et al. "Size-Based Differentiation of Cancer and Normal Cells by a Particle Size Analyzer Assisted by a Cell-Recognition PC Software". In: *Biological and Pharmaceutical Bulletin* 41.4 (2018), pp. 487–503. DOI: 10.1248/bpb.b17-00776.

[83] Angelyn Nguyen et al. "Stiffness of pancreatic cancer cells is associated with increased invasive potential". In: *Integr. Biol.* 8 (Oct. 2016). DOI: 10.1039/C6IB00135A.

[84] T Ushiki. "[The three-dimensional ultrastructure of the collagen fibers, reticular fibers and elastic fibers: a review]". In: *Kaibogaku zasshi. Journal of anatomy* 67.3 (June 1992), pp. 186–199. ISSN: 0022-7722. URL: http://europepmc.org/abstract/MED/1523957.

[85] Ibiayi Dagogo-Jack and Alice T. Shaw. "Tumour heterogeneity and resistance to cancer therapies". In: *Nature Reviews Clinical Oncology* 15.2 (Feb. 2018), pp. 81–94. ISSN: 1759-4782. DOI: 10.1038/nrclinonc.2017.166. URL: https://doi.org/10.1038/nrclinonc.2017.166.

[86] Malin Jansson et al. "Prognostic Value of Stromal Type IV Collagen Expression in Small Invasive Breast Cancers". In: *Frontiers in Molecular Biosciences* 9 (2022). DOI: 10.3389/fmolb.2022.904526. URL: https://www.frontiersin.org/articles/10.3389/fmolb.2022.904526.

APPENDICES

A MATLAB script for image analysis of SWE images

The following MATLAB script was used to analyze the images from shear wave elastography. The first part of the code was provided by Rune Hansen and Naseh Amini, and displays three images showing the B-mode image of the tumor, the shear wave velocity, and standard deviation of measurements, as shown in Figure 3.4.1. The second part prompts the user to draw the ROI in the B-mode image, and converts the mask to the two other images. Within the ROI in the shear wave velocity image, the mean and median value is calculated, in addition to the standard deviation and variance. This provides the mean and median shear velocity, in addition to SD and variance. The tumor tag refers to a specific measurement, where the first three numbers refers to the tumor number, the fourth number refers to the measurement number, and the last number refers to whether it is measurements of waves propagation to the right (1) or left (2).

```
if exist( 'replaceTag', 'var') && replaceTag
    disp('Using set tumortag');
    replaceTag = 0;
else
    tumortag = '19611';
end

fid = fopen(['meta' tumortag '.txt']);
test = textscan(fid, '%f %f');
fclose(fid);

% shearSize = [240 30];
% bmodeSize = [240 447];
% zaxis_lims = [0.0066 0.0176];
% xaxisS_lims = [-0.00585 0.00575];
% xaxisB_lims = [-0.01115 0.0112];


shearSize = [test{1}(1) test{2}(1)];
bmodeSize = [test{1}(2) test{2}(2)];
zaxis_lims = [test{1}(3) test{2}(3)];
xaxisS_lims = [test{1}(4) test{2}(4)];
```

```
xaxisB_lims = [test{1}(5) test{2}(5)];



fid = fopen( ['shear' tumortag] );
shearImg = fread( fid, 'single');
fclose(fid);
shearImg = reshape( shearImg, shearSize);

fid = fopen( ['bmode' tumortag] );
bmodeImg = fread( fid, 'single');
fclose(fid);
bmodeImg = reshape( bmodeImg, bmodeSize);

fid = fopen( ['std' tumortag] );
stdImg = fread( fid, 'single');
fclose(fid);
stdImg = reshape( stdImg, [shearSize]);
% stdImg = stdImg

%%
fig10 = figure(10);
subplot(3,1,1), imagesc( xaxisB_lims*1e3, zaxis_lims*1e3,
   bmodeImg); xlabel('[mm]'); ylabel('[mm]')
daspect([1, 1, 1]);
subplot(3,1,2), imagesc( xaxisS_lims*1e3, zaxis_lims*1e3,
   shearImg); caxis([1 8]); xlabel('[mm]'); ylabel('[mm]')
daspect([1, 1, 1]);
subplot(3,1,3), imagesc( xaxisS_lims*1e3, zaxis_lims*1e3,
   stdImg); xlabel('[mm]'); ylabel('[mm]')
daspect([1, 1, 1]);

%% Mark ROI in bmodeImg
fig11 = figure(11);
imagesc(xaxisB_lims * 1e3, zaxis_lims * 1e3, bmodeImg);
xlabel('[mm]');
ylabel('[mm]');
title('Select␣ROI␣in␣B-mode␣Image');
axis image;
colormap gray;

% Allow the user to draw a freehand ROI
h = imfreehand(gca);
mask = h.createMask();

% Apply the ROI mask to the bmodeImg
roiBmodeImg = bmodeImg .* mask;

% Display the ROI in a separate figure
fig12 = figure(12);
imagesc(xaxisB_lims * 1e3, zaxis_lims * 1e3, roiBmodeImg);
```

```
xlabel('[mm]');
ylabel('[mm]');
title('Region of Interest (ROI)');

%% Apply ROI to shearImg and stdImg
% Account for different axis sizes
scaleFactor = size(bmodeImg) ./ size(shearImg);

% Resize the mask to match shearImg size
resizedMask = imresize(mask, size(shearImg)) > 0;

% Apply the resized mask to shearImg
roiShearImg = shearImg .* resizedMask;

% Apply the resized mask to stdImg
roiStdImg = stdImg .* resizedMask;

%% Display images and statistics
fig13 = figure(13);
subplot(3, 1, 1), imagesc(xaxisB_lims * 1e3, zaxis_lims * 1e3
    , roiBmodeImg);
xlabel('[mm]');
ylabel('[mm]');
title('Region of Interest (ROI) in B-mode Image');
subplot(3, 1, 2), imagesc(xaxisS_lims * 1e3, zaxis_lims * 1e3
    , roiShearImg);
caxis
subplot(3, 1, 3), imagesc(xaxisS_lims * 1e3, zaxis_lims * 1e3
    , roiStdImg);
xlabel('[mm]');
ylabel('[mm]');
title('Region of Interest (ROI) in Standard Deviation Image')
    ;

%% Calculate statistics within ROI from shearImg
roiValuesShear = roiShearImg(resizedMask);
meanValueShear = mean(roiValuesShear);
medianValueShear = median(roiValuesShear);
stdValueShear = std(roiValuesShear);
varValueShear = var(roiValuesShear);
numValuesShear = numel(roiValuesShear);

fprintf('Statistics within ROI from Shear Image:\n');
fprintf('Number of values: %d\n', numValuesShear);
fprintf('Mean: %.4f\n', meanValueShear);
fprintf('Median: %.4f\n', medianValueShear);
fprintf('Standard Deviation: %.4f\n', stdValueShear);
fprintf('Variance: %.4f\n', varValueShear);
```

B Python script for analyzing indentation force curves

The following Python script was used to correct indentation force curves for DPBS evaporation, and curve fitting of Hooke's law and Hertz model. The script also estimates spring constant and Young's modulus from curve fitting. The script assumes a tip diameter of 1 mm, and a biological sample with Poisson ratio 0.5. The script also calculates the P-value and R^2.

```
#Import packages

import numpy as np
import matplotlib.pyplot as plt
from sklearn.metrics import r2_score
from scipy.optimize import curve_fit
from scipy.stats import t, sem

#Defining DPBS correction line

def p(x):
    return -0.27378543*x - 0.00000193

#Defining Hertz model and Hooke's law

def hertz_law(d, E):
    return (((4/3)*E)/(1-(0.5**2)))*(np.sqrt(0.5*0.001)*(d)
       **(3/2))

def hookes_law(x, k):
    return k*x

def plot(file, plotlabel, min, max):
    plt.rcParams.update({'font.size':10})
    depth = np.loadtxt(file, dtype=float, usecols=[0])
    depth *= 1E-3
    force = np.loadtxt(file, dtype=float, usecols=[1])
    force *= 0.0098
    correctedforce = force-p(depth)
    plt.figure(figsize=(10,6))
    plt.plot(depth, correctedforce, label = plotlabel, color=
       'C3')

    #Model fitting

    popt_hertz, pcov_hertz = curve_fit(hertz_law, depth,
       correctedforce)
    F_hertz = hertz_law(depth, *popt_hertz)

    popt_hookes, pcov_hookes = curve_fit(hookes_law, depth,
       correctedforce)
    F_hookes = hookes_law(depth, *popt_hookes)
```

```
39
40      mask = (depth >= 0.0001) & (depth <= 0.0002)
41      depth_interval = depth[mask]
42      force_interval = correctedforce[mask]
43      popt_hookes_interval, pcov_hookes_interval = curve_fit(
           hookes_law, depth_interval, force_interval)
44      F_hookes_interval = hookes_law(depth_interval, *
           popt_hookes_interval)
45
46      #Find Young's modulus and spring constant
47
48      youngsmodulus = popt_hertz[0]
49      youngsmodulus_kpa = popt_hertz[0]*1E-3
50      springconstant = popt_hookes[0]
51      springconstant_hookes_interval = popt_hookes_interval[0]
52
53      #Calculating R squared
54
55      r_squared_hertz = r2_score(correctedforce, F_hertz)
56      r_squared_hookes = r2_score(correctedforce, F_hookes)
57      r_squared_hookes_interval = r2_score(y_interval,
           hookes_law(x_interval, *popt_hookes_interval))
58
59      #Calculating P-value
60
61      residuals = correctedforce - hertz_law(depth, *popt_hertz
           )
62      degrees_of_freedom = len(correctedforce) - len(popt_hertz
           )
63      p_value_hertz = 2 * (1 - t.cdf(np.abs(residuals).mean() /
            np.std(residuals), degrees_of_freedom))
64
65      residuals = correctedforce - hookes_law(x, *popt_hookes)
66      degrees_of_freedom = len(y_corrected) - len(popt_c)
67      p_value_hookes = 2 * (1 - t.cdf(np.abs(residuals).mean()
           / np.std(residuals), degrees_of_freedom))
68
69      residuals = force_interval - hookes_law(depth_interval, *
           popt_hookes_interval)
70      degrees_of_freedom = len(force_interval) - len(
           popt_hookes_interval)
71      p_value_hookes_interval = 2 * (1 - t.cdf(np.abs(residuals
           ).mean() / np.std(residuals), degrees_of_freedom))
72
73      #Plot model fits
74
75      plt.plot(x, F_hertz, color='C1', linestyle='dashdot',
           label=f'Hertz␣law␣fit:␣E={popt_hertz_c[0]*1E-3:.2g}␣
           kPa')
76      plt.plot(x, F_hookes, color='C0', linestyle='dashed',
           label=f'Hooke\'s␣law␣fit:␣k={popt_c[0]:.2g}␣N/m')
```

```
77      x__intervalplot = np.linspace(x_interval.min(),
            x_interval.max(), 100)
78      plt.plot(x_plot_interval, F_hookes_interval, color='C2',
            linestyle='dashed', label=f"Hooke's␣law␣fit␣within␣
            linear␣interval:␣k␣=␣{slope:.2g}␣N/m")
79
80      #Extend the plot outside the interval
81
82      x_plot_extended = np.linspace(depth.min(), depth.max(),
            100)
83      y_fit_extended = slope * x_plot
84      plt.plot(x_plot, y_fit_extended, color='C2', linestyle='
            dashed')
85
86
87
88      plt.legend(fontsize=10, ncol=1)
89      plt.tight_layout(pad=2)
90      plt.grid(which = "major", linewidth = 1)
91      plt.grid(which = "minor", linewidth = 0.2)
92      plt.minorticks_on()
93      plt.xlabel("Indentation␣depth␣(\u03BCm)", fontsize=12)
94      plt.ylabel("Load␣(mN)", fontsize=12)
95      x1 = [0,0.00005,0.00010,0.00015,0.00020,0.00025]
96      squad = ['0','50','100','150','200','250']
97      plt.xticks(x1, squad)
98
99      plt.show()
100
101     with open('YoungsModulus.txt', 'a') as f:
102         f.write(str(youngsmodulus_kpa) + '\n')
103     with open('Pvalue_hertz.txt', 'a') as f:
104         f.write(str(p_value_hertz) + '\n')
105     with open('Rsquared_hertz.txt', 'a') as f:
106         f.write(str(r_squared_hertz) + '\n')
107
108     with open('SpringConstant.txt', 'a') as f:
109         f.write(str(springconstant) + '\n')
110     with open('Pvalue_hookes.txt', 'a') as f:
111         f.write(str(p_value_hookes) + '\n')
112     with open('Rsquared_hookes.txt', 'a') as f:
113         f.write(str(r_squared_hookes) + '\n')
114
115     with open('SpringConstantInterval.txt', 'a') as f:
116         f.write(str(springconstant_hookes_interval) + '\n')
117     with open('Pvalue_Hookes_Interval.txt', 'a') as f:
118         f.write(str(p_value_hookes_interval) + '\n')
119     with open('Rsquared_Hookes_Interval.txt', 'a') as f:
120         f.write(str(r_squared_hookes_interval) + '\n')
```

C Table of tumors, including weights and dimensions

This project used six KPC, six 4T1 and six CT26 tumors. Table C.1 show the animal ID of the animals from which they were harvest from, as well as the weight and dimensions of the tumors, which was measured right after harvesting.

Table C.1: Tumors used in the project, with weights and dimensions, and the ID of the animal from which they were harvested from.

Tumor type	**Animal ID**	**Tumor size (mm)**	**Tumor weight (g)**
KPC	169	6.2 x 5.9 x 4.8	0.1493
KPC	170	7.55 x 6.2 x 5.0	0.1692
KPC	171	7 x 4.5 x 3.7	0.0751
KPC	172	5.6 x 5.9 x 4.1	0.1024
KPC	173	5 x 5.2 x 2.2	0.0393
KPC	174	5.4 x 5.2 x 3.3	0.0670
4T1	175	10.2 x 8.4 x 6.3	0.3902
4T1	176	9.8 x 11.9 x 6.2	0.4231
4T1	177	10.1 x 8.2 x 6.6	0.4781
4T1	178	9.7 x 10 x 7.6	0.5766
4T1	179	9.8 x 7.7 x 5.1	0.2909
4T1	180	10.1 x 8.5 x 6.5	0.4182
CT26	184	10 x 9.4 x 6	0.3950
CT26	185	9.7 x 8.5 x 6.7	0.4328
CT26	186	6.9 x 5.5 x 4.7	0.1384
CT26	190	11.2 x 9.5 x 6.2	0.5715
CT26	191	11 x 10 x 6.3	0.4580
CT26	196	10.2 x 8.6 x 6.11	0.4387

D Outliers

Table D.1 shows the values of the outliers removed by Prism using the ROUT outlier detection method, with Q=1%. The table also shows which tumor model it originates from. No outliers were found in the sGAG data set.

Table D.1: The values of the outliers removed by ROUT method, and the tumor model from which they originate from.

Spring constant	
Tumor model	**Spring constant (N/m)**
CT26	3.238
Young's modulus (Hertz)	
Tumor model	**Young's modulus (kPa)**
CT26	6.145
Young's modulus (SWE)	
Tumor model	**Young's modulus (kPa)**
4T1	106.236
4T1	119.865
4T1	101.282
4T1	114.199
Collagen concentration	
Tumor model	**Collagen concentration (μg/mg)**
CT26	0.909
CT26	0.906
CT26	1.001
CT26	1.002
CT26	1.848
CT26	1.851

Figure D.1 show the force curve corresponding to the outlier removed from the data set, and the corresponding curves from Hooke's law and Hertz model curve fitting.

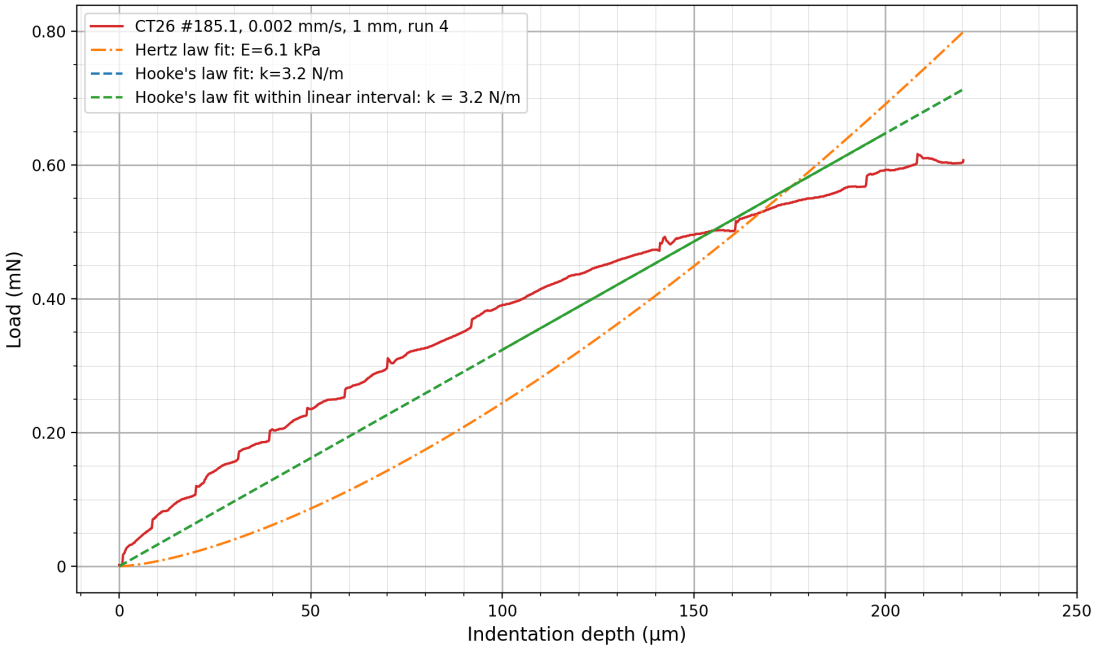

Figure D.1: The corresponding force curve to the outlier removed from the indentation data set. The red line is the force curve, corrected for DPBS evaporation. The orange curve is the Hertz model fit. The blue and green curves are the Hooke's law model fit curves, calculated for the entire force curve and within the interval 100 to 200 μm indentation depth, respectively. All indentation experiments were performed with an indenter with r = 0.5 mm, at 0.002 mm/s speed, with 200μm indentation depth.

E Hooke's law model fit for entire force curve

Figure E.1 shows the spring constant for all three tumor models, measured in N/m. The spring constant is derived from the model fit of Hooke's law to the entire force curve. KPC has a significantly higher spring constant than both 4T1 and CT26. There is no statistical significance between 4T1 and CT26, meaning their spring constants are similar. The min-max range, median, mean and standard deviation of the spring constant were found to be [2.371 - 6.098, 4.145, 4.183 $\pm$ 1.120] for KPC, [0.620 - 3.313, 1.377, 1.542 $\pm$ 0.747] for 4T1, and [0.420 - 2.220, 0.870, 0.910 $\pm$ 0.375] for CT26.

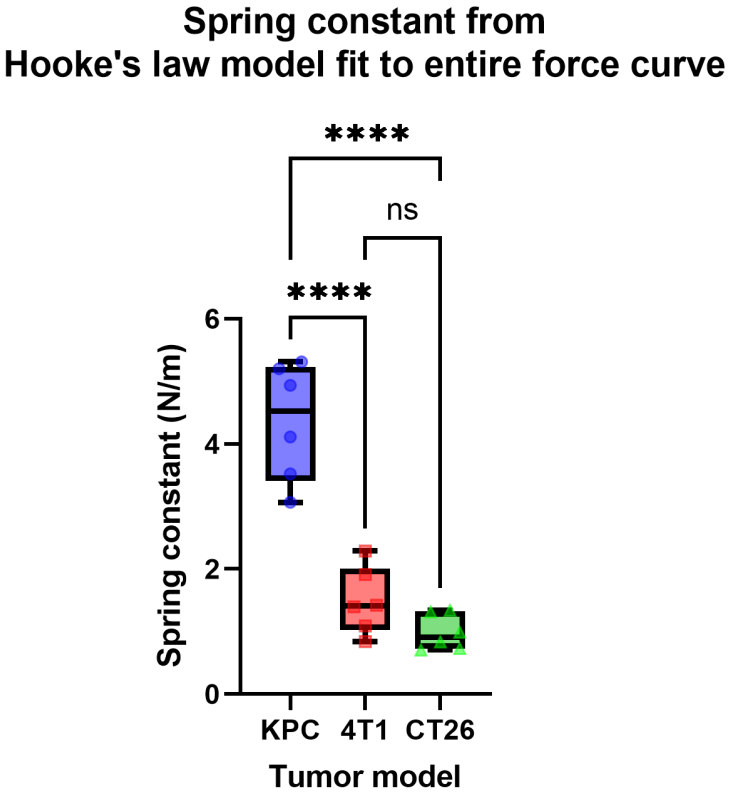

Figure E.1: The spring constant of the tumor models in a box plot. Whiskers represents the minimum and maximum values, and the box is the 25-75%. The median is depicted by a horizontal line crossing the box. Each individual point within the box plot represents the mean value of one tumor. The presence of asterisks between the boxes indicates the statistical significance between the respective data sets, as explained in Table 3.6.1.

F Intra- vs Interheterogeneity

Table F.1 shows the calculated intra- and interheterogeneity within tumor model populations, and the relative contribution of intraheterogeneity to the total tumor heterogeneity. The calculations are performed as described in Section 2.4.

Table F.1: The intra- (σ^2_{intra}) and interheterogeneity (σ^2_{inter}) within the tumor model populations, and the relative contribution of intraheterogeneity to the total tumor heterogeneity (f). Calculations were performed for data sets from indentation, SWE, and measurements of collagen and sGAG concentrations.

Tumor type	σ^2_{inter}	σ^2_{intra}	f
Spring constant			
KPC	1.204	0.638	0.346
4T1	0.550	0.396	0.419
CT26	0.139	0.122	0.468
Young's modulus (Hertz)			
KPC	4.979	2.499	0.334
4T1	2.196	1.570	0.417
CT26	0.492	0.460	0.483
Young's modulus (SWE)			
KPC	8.084	7.302	0.475
4T1	9.964	5.434	0.353
CT26	70.558	21.860	0.237
Collagen concentration			
KPC	1.120	0.746	0.400
4T1	1.364	0.682	0.333
CT26	0.017	0.015	0.462
sGAG concentration			
KPC	0.415	0.389	0.483
4T1	0.532	0.855	0.617
CT26	2.608	1.311	0.334

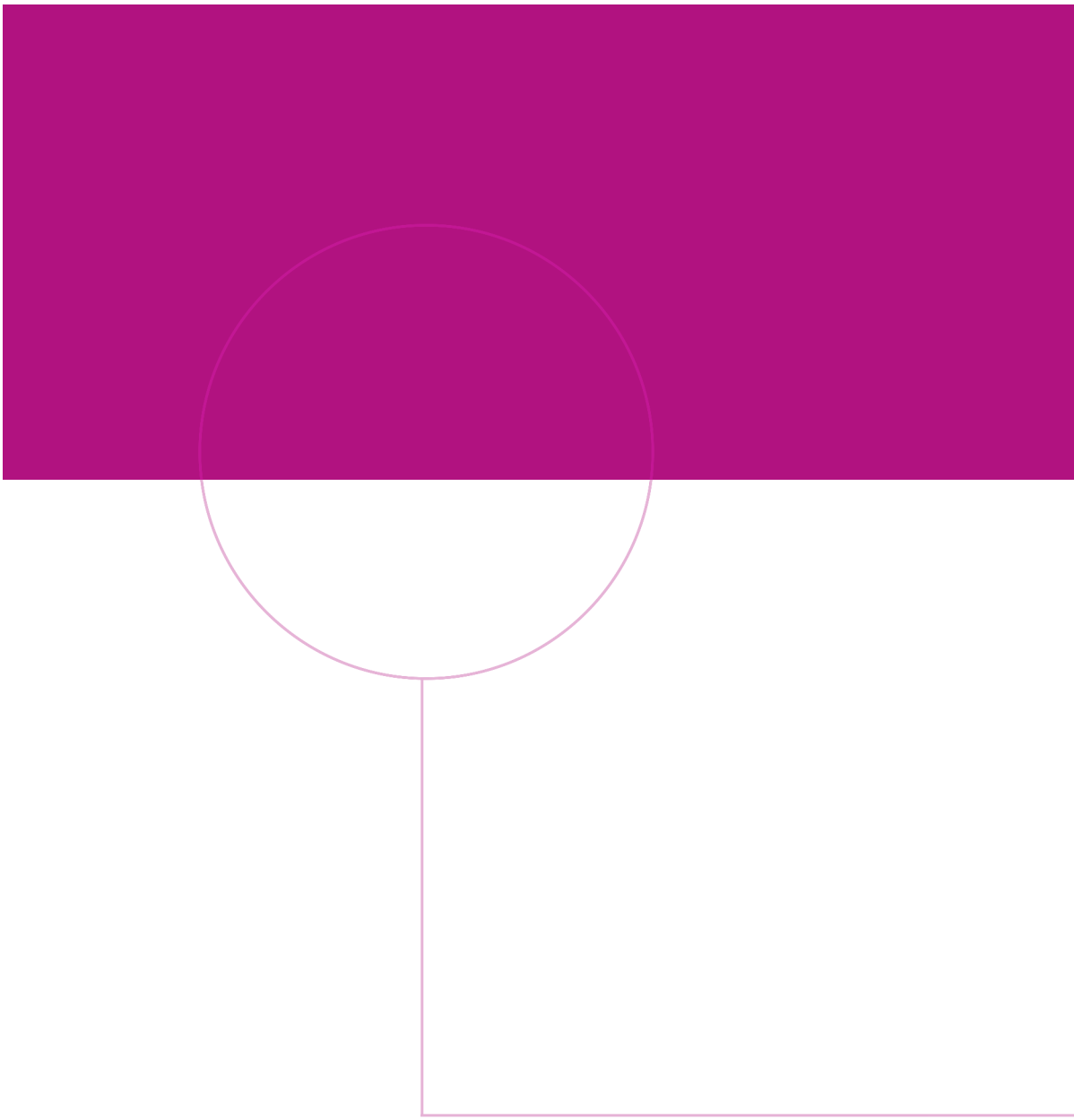

NTNU

Norwegian University of
Science and Technology